Two C-terminal sequence variations determine differential neurotoxicity between human and mouse α-synuclein

Natalie Landeck,[1,¶] Katherine E. Strathearn,[2, ¶, #a] Daniel Ysselstein,[2, ¶] Kerstin Buck,[1, #b], Sayan Dutta,[2,3] Siddhartha Banerjee,[4] Zhengjian Lv,[4, #c] John D. Hulleman,[2, #d] Jagadish Hindupur,[2, #e] Li-Kai Lin,[5] Sonal Padalkar,[5, #f] George P. McCabe,[6] Lia A. Stanciu,[5] Yuri L. Lyubchenko,[4] Deniz Kirik,[1,*] and Jean-Christophe Rochet[2,3,*]

[1]Brain Repair and Imaging in Neural Systems, Department of Experimental Medical Science, Lund University, Lund, Sweden

[2]Department of Medicinal Chemistry and Molecular Pharmacology, Purdue University, West Lafayette, IN, USA

[3]Purdue Institute for Integrative Neuroscience, Purdue University, West Lafayette, IN, USA

[4]Department of Pharmaceutical Sciences, University of Nebraska Medical Center, Omaha, NE, USA

[5]Department of Materials Engineering, Purdue University, West Lafayette, IN, USA

[6]Department of Statistics, Purdue University, West Lafayette, IN, USA

[¶]These authors contributed equally to this work

[#a]Current address: Oxford Genetics Ltd., USA
[#b]Current address: AbbVie Deutschland GmbH & Co KG, Ludwigshafen, Germany
[#c]Current address: Bruker Nanosurfaces Division, Goleta, Santa Barbara, CA, USA
[#d]Current address: Departments of Ophthalmology and Pharmacology, University of Texas Southwestern Medical Center, Dallas, TX, USA
[#e]Current address: Liveon Biolabs Pvt. Ltd., Tumakuru, Karnataka, India
[#f]Current address: Department of Mechanical Engineering, Iowa State University, Ames, IA, USA

*Correspondence: deniz.kirik@med.lu.se (D.K.), jrochet@purdue.edu (J.-C.R.)

Abstract

α-Synuclein (aSyn) aggregation is thought to play a central role in neurodegenerative disorders termed synucleinopathies, including Parkinson's disease (PD). Mouse aSyn contains a threonine residue at position 53 that mimics the human familial PD substitution A53T, yet in contrast to A53T patients, mice show no evidence of aSyn neuropathology even after aging. Here we studied the neurotoxicity of human A53T, mouse aSyn, and various human-mouse chimeras in cellular and *in vivo* models as well as their biochemical properties relevant to aSyn pathobiology. We report that mouse aSyn is less neurotoxic than the human A53T variant as a result of inhibitory effects of two C-terminal amino acid substitutions on membrane-induced aSyn aggregation and aSyn-mediated vesicle permeabilization. Our findings highlight the importance of membrane-induced self-assembly in aSyn neurotoxicity and suggest that inhibiting this process by targeting the C-terminal domain could slow neurodegeneration in PD and other synucleinopathy disorders.

Introduction

Parkinson's disease (PD) is a common progressive neurodegenerative disorder characterized clinically by motor symptoms attributed to a loss of dopaminergic neurons in the *substantia nigra* (SN). At post-mortem examination neurons in various brain regions of PD patients present with cytosolic inclusions named Lewy bodies that contain amyloid-like fibrils of the presynaptic protein α-synuclein (aSyn) (1). A number of patients with familial forms of PD have been found to harbor mutations in the SNCA gene, including point mutations encoding the substitutions A30P, E46K, H50Q, G51D, A53E, and A53T and gene multiplications (2). Genetic and neuropathological findings in humans and data from animal model studies suggest that aSyn self-assembly plays a central role in the pathogenesis of PD and other neurodegenerative disorders involving an accumulation of aSyn aggregates in the brain, collectively referred to as synucleinopathies (3). A detailed understanding of molecular mechanisms by which aSyn forms neurotoxic aggregates is critical for developing therapies aimed at slowing neurodegeneration in the brains of patients with PD and other synucleinopathy disorders.

aSyn has been reported to adopt a natively unfolded, monomeric structure in solution (4) and to exist as a compact disordered monomer in mammalian cells (5), although additional evidence suggests that it can also exist as an oligomer in the cytosol (6). The protein is typically expressed as a 14.4 kDa polypeptide and consists of 3 domains. The N-terminal domain spanning residues 1-67 contains five conserved, lysine-rich repeats. The central region spanning residues 61-95 contains a sixth lysine-rich repeat and is highly hydrophobic. A key feature of this region is the presence of a segment spanning residues 71-82 that is required for aSyn aggregation (7). The C-terminal region spanning residues 96-140 is enriched with proline and acidic residues and is thought to regulate aSyn aggregation through auto-inhibitory long-range interactions (8, 9), with electrostatic interactions mediated by the acidic residues playing a

major role in increasing the fibrillization lag time (10). aSyn binds to anionic phospholipid vesicles by forming an amphipathic α-helix with varying lengths, including a short N-terminal helix spanning residues ~1-25 and a longer helix spanning residues ~1-97 encompassing both the N-terminal and central hydrophobic domains (11, 12). Although membrane binding apparently plays an important role in the normal function of aSyn related to regulation of synaptic vesicle trafficking (12, 13), the protein has also been shown to undergo accelerated aggregation when incubated in the presence of phospholipid vesicles at high protein:lipid ratios (14-16). aSyn aggregation at the membrane surface is likely stimulated by the exposure of hydrophobic residues as the membrane-bound protein shifts from the long-helix form to the short-helix form (11, 16), and by the fact that molecular interactions needed for aSyn self-assembly likely occur with a higher probability on the two dimensional surface of the lipid bilayer than in solution (17, 18). Evidence from our laboratory suggests that membrane-induced aSyn aggregation plays a key role in neurotoxicity (16), potentially via a mechanism involving membrane permeabilization (19-22).

An interesting observation regarding aSyn biology is the fact that mouse aSyn (m-aSyn) naturally contains a threonine residue at position 53 and is thus identical to the human familial PD mutant A53T (h-aSyn A53T) at this site (23). This observation raises the question of why h-aSyn A53T triggers accelerated neurodegeneration in the brains of familial PD patients, whereas even aged mice show no evidence of neurodegeneration or the presence of Lewy bodies (24). This paradox is particularly striking given that recombinant m-aSyn forms amyloid-like fibrils more rapidly than h-aSyn WT or h-aSyn A53T (25, 26), apparently as a result of the disruption of long-range interactions involving the C-terminal region and the N-terminal and central hydrophobic domains (27). In fact, however, m-aSyn differs from h-aSyn-A53T by six mismatches, one in the central hydrophobic domain (S87N) and five in the C-terminal region (L100M, N103G, A107Y, D121G and D122S) (Figure 1A), and each of these could contribute to the apparent difference in neurotoxicity between the two variants.

The goal of this study was to investigate the impact of the mismatches between m-aSyn and h-aSyn A53T on aSyn neurotoxicity. Previously it was reported that rat aSyn (which differs from the mouse protein by a single G-to-S mismatch at position 121) failed to trigger neuronal cell death when expressed from a lentiviral vector infused in rat SN, in contrast to h-aSyn WT and h-aSyn A53T (28). Similarly, we found that rat aSyn had a reduced ability to trigger nigral dopaminergic cell death compared to h-aSyn A53T in the rAAV-mediated overexpression model in the rat (29). Based on the close sequence similarity between mouse and rat aSyn, we hypothesized that the mouse protein is less neurotoxic than h-aSyn A53T, potentially because the toxic consequences of having a threonine residue at position 53 are alleviated by mismatch residues elsewhere in the murine sequence. To address this hypothesis, we compared h-aSyn A53T, m-aSyn, and various human-mouse chimeras in terms of their ability to elicit neurodegeneration in cellular and animal models relevant to PD and other synucleinopathy disorders. The human and mouse proteins and a subset of chimeras were further examined for their ability to form amyloid-like fibrils in the absence of membranes, undergo membrane-induced aSyn aggregation, and trigger membrane permeabilization.

Results

Neurotoxicity of aSyn variants in primary midbrain culture

In the first part of our study, we used a primary mesencephalic cell culture model to examine the effects of amino acid variations between m-aSyn and h-aSyn A53T on aSyn neurotoxicity. In addition to h-aSyn A53T and m-aSyn, two chimeric variants were analyzed: (i) h-aSyn Chimera, consisting of h-aSyn with the human-to-mouse substitutions A53T, D121G, and N122S; and (ii) m-aSyn Chimera, consisting of m-aSyn with the mouse-to-human substitutions G121D and S122N (Figure 1B). We chose to examine the effects of substitutions at positions 121 and 122 based on data showing that post-translational modifications near these

residues, including C-terminal truncation and Y125 phosphorylation, modulate the protein's aggregation propensity and neurotoxicity (30-34).

Primary midbrain cultures were processed as untreated control or transduced with adenovirus encoding each of the aSyn variants at multiplicities of infection (MOIs) that were adjusted to ensure equal expression of the different variants. We have previously shown that the adenoviral transduction efficiency is >90% for dopaminergic and non-dopaminergic neurons (16). The cells were fixed and stained for microtubule associated protein 2 (MAP2), a general neuronal marker, and tyrosine hydroxylase (TH), a marker of dopaminergic neurons. Relative dopaminergic cell viability was evaluated by determining the percentage of $MAP2^+$ neurons that were also TH^+. We found a significant reduction in the percentage of TH^+ neurons in cultures transduced with h-aSyn A53T virus compared to untreated cultures or cultures expressing m-aSyn (Figure 2A, B). Cultures expressing m-aSyn Chimera exhibited a decrease in relative TH^+ cell viability, similar to A53T-expressing cultures (Figure 2B). In contrast, h-aSyn Chimera had no impact on dopaminergic cell survival, similar to m-aSyn (Figure 2A). In additional experiments we found that cultures expressing A53T/D121G (but not A53T/N122S) exhibited a significant decrease in TH^+ neuron loss compared to cultures expressing A53T (Figure 2C). Together these results suggested that (i) h-aSyn A53T is more neurotoxic than m-aSyn, and (ii) the human-to-mouse substitutions D121G and N122S (and in particular D121G) are at least partially responsible for the decrease in neurotoxicity of m-aSyn compared to h-aSyn A53T.

In an independent set of experiments, we examined the impact of the mismatch between m-aSyn and h-aSyn A53T at position 87 (Figure 1) on aSyn-mediated dopaminergic cell death. Here our rationale was that residue 87 is located in the central hydrophobic domain, and substitutions and deletions in this region have been shown to modulate aSyn aggregation and neurotoxicity (7, 31). Cultures expressing h-aSyn A53T/S87N, h-aSyn Chimera S87N, or m-aSyn Chimera N87S exhibited no difference in relative dopaminergic cell viability compared to cultures expressing h-aSyn A53T (Figure 2D), h-aSyn Chimera (Figure 2E), or m-aSyn Chimera

102 (Figure 2F), respectively. From these results, we inferred that the mismatch between m-aSyn
103 and h-aSyn A53T at position 87 does not affect aSyn neurotoxicity.
104 Taken together, these findings suggest that residues D121 and N122 are important for
105 the ability of h-aSyn A53T to elicit dopaminergic cell death. Moreover, we infer that residues
106 G121 and S122 (but not N87) of m-aSyn interfere with the expected neurotoxic effect of the
107 threonine residue at position 53 of the mouse sequence.
108
109 **Neurotoxicity of aSyn variants in rat nigrostriatal projection neurons**
110 To further examine the effects of mismatches at positions 121 and 122 of m-aSyn and h-
111 aSyn A53T on aSyn neurotoxicity, we characterized h-aSyn A53T, m-aSyn, h-aSyn Chimera,
112 and m-aSyn Chimera in terms of their toxicity to nigral dopamine neurons *in vivo*. rAAV vectors
113 encoding these variants were injected unilaterally into the rat SN at two different titers,
114 corresponding to a low-toxicity titer at 1.3E13 gc/mL (n=4-6 per group) and a high-toxicity titer at
115 3.5E14 gc/mL (n=4-10 per group). Animals were killed 8 weeks after transduction, and serial
116 coronal midbrain sections were stained for histological analysis to assess transgene expression
117 and the extent of neurodegeneration in the nigral dopamine neurons. Representative specimens
118 of animals injected with a high-titer vector are shown in Figure 3A-Y. The aSyn antibody applied
119 here was used to evaluate transgene expression and is specific for aSyn but does not
120 distinguish between human and rodent variants as seen in Figure 3A, where endogenous aSyn
121 can be visualized especially in the axon terminal located in the SN pars reticulata contralateral
122 to the AAV injection. On the injected side, transduced cells over-expressing h-aSyn A53T
123 (Figure 3B), h-aSyn Chimera (Figure 3C), m-aSyn (Figure 3D), or m-aSyn Chimera (Figure 3E)
124 were visible in the SN pars compacta. The human aSyn-specific syn211 antibody resulted in
125 specific staining in groups expressing h-aSyn A53T or m-aSyn Chimera, whereas the
126 contralateral side of rat midbrain sections as well as in sections expressing m-aSyn or h-aSyn
127 Chimera were devoid of any immunoreactivity (Figure S1). Notably, staining with a pan aSyn

128 antibody, Syn-1, showed that the overexpression was present in all groups, suggesting that the
129 affinity of syn211 to the aSyn variants was dependent on the identity of the residues at positions
130 121 and 122 (Figure S1F-J).

131 Immunohistochemical analyses were carried out to evaluate the loss of dopaminergic
132 neurons in rat midbrain sections stained for TH (Figure 3F-J) and vesicular monoamine
133 transporter 2 (VMAT2) (Figure 3K-O). A clear loss of TH^+ as well as $VMAT2^+$ neurons was seen
134 in all groups when compared to the uninjected contralateral side (Figures 3F and 3K,
135 respectively). The reduction in cell numbers was not due to a loss of expression of
136 dopaminergic markers, as it was clearly visible also in specimens stained with antibodies
137 against the neuronal marker proteins Hu (Figure 3P-T) or with cresyl violet (CV) (Figure 3U-Y).
138 In order to quantify dopaminergic cell loss in the SN, we counted TH^+ cells in serial sections
139 from both the low-titer and high-titer vector groups. Results obtained for the low-titer group
140 showed no cell death for any of the aSyn variants and no significant differences among groups
141 (Figure 3Z). In contrast, in the 3.5E14 gc/mL titer groups, the expression of h-aSyn A53T
142 resulted in a significantly higher percentage of cell death when compared to the h-aSyn
143 Chimera group (75 ± 4 versus 50 ± 5% cell loss, respectively; Figure 3AA). Moreover, the m-
144 aSyn group displayed significantly reduced neurotoxicity in TH^+ neurons than the m-aSyn
145 Chimera group (56 ± 8 versus 17 ± 3% cell survival, respectively). These results suggested a
146 considerable effect of the human/mouse mismatches at positions 121 and 122 on aSyn-
147 mediated dopaminergic cell death in rat SN.

148 To determine whether the significant differences in dopaminergic cell death observed in
149 the SN were also evident in the nigrostriatal projections, we evaluated the TH^+ and $VMAT2^+$
150 fiber intensity in the striatum of the high titer groups. In serial sections throughout the
151 rostocaudal axis of the striatum, we found a reduction in staining intensity for both TH (Figure
152 4A-E, A'-E') and VMAT2 (Figure 4G-K, G'-K') for all groups when compared to contralateral
153 striatal areas. A significant reduction of innervation density was observed for the m-aSyn

154 Chimera group when compared to the m-aSyn group for both TH^+ (Figure 4F) and $VMAT2^+$
155 projections (Figure 4L). These observations are in accordance with dopaminergic cell loss seen
156 in the corresponding SN sections of the same animals. There was a trend for a difference in the
157 h-aSyn Chimera group when compared to the h-aSyn A53T group, although this did not reach
158 significance [TH (p=0.11); VMAT2 (p=0.27)].
159

160 **Aggregate formation by aSyn variants in rat midbrain**

161 To determine whether the aSyn variants differed in terms of aggregation propensity in rat
162 midbrain, we treated striatal sections with Proteinase K (PK) to digest non-aggregated species
163 and reveal digestion-resistant aSyn assemblies. As a reference for the PK incubation we chose
164 the endogenous aSyn staining in the CA3 region of the hippocampus (Figure S2A, F, K), which
165 would not be affected by nigral transduction. Whereas untreated striatal sections stained for
166 aSyn showed both punctate and fiber-like staining (Figure S2B-E), a clearance of digested and
167 therefore non-aggregated aSyn could already be appreciated after 5 min of PK incubation
168 (Figure S2F-J). At a later incubation time (45 min) when endogenous aSyn staining could no
169 longer be detected in the CA3 region (Figure S2K), and therefore all non-aggregated synuclein
170 would be digested, resistant aSyn aggregates were detected in striatal sections in all groups
171 (Figure S2L-O). These results suggested that the human/mouse mismatches at positions 121
172 and 122 do not have a major impact on the ability of aSyn to form PK-resistant aggregates in
173 the striatal fiber terminals of dopaminergic neurons.
174

175 **Effects of human/mouse aSyn mismatches on aSyn fibrillization rates**

176 The next set of experiments was aimed at determining the effects of human/mouse aSyn
177 mismatches on rates of aSyn fibrillization. Based on evidence that m-aSyn forms amyloid-like
178 fibrils more rapidly than h-aSyn WT or A53T (25, 26), we hypothesized that a more rapid
179 conversion of natively unfolded aSyn to mature, amyloid-like fibrils could lead to a depletion of

180 toxic oligomers (26, 35, 36). As a corollary, we reasoned that the human-to-mouse substitutions
181 could stimulate aSyn fibrillization, which in turn could account for the reduced neurotoxicity of m-
182 aSyn and h-aSyn Chimera compared to h-aSyn A53T. To address this hypothesis, we
183 monitored the fibrillization of human, mouse, and chimeric aSyn variants using a thioflavin T
184 fluorescence assay. Consistent with previous results, we found that m-aSyn and h-aSyn A53T
185 formed fibrils with a markedly reduced lag time compared to h-aSyn WT, although the decrease
186 in lag time was more pronounced for the mouse protein (Figure 5A). Analysis of the chimeric
187 aSyn variants revealed that h-aSyn Chimera formed fibrils with a longer lag time compared to h-
188 aSyn A53T, whereas the rate of fibrillization was only slightly decreased for m-aSyn Chimera
189 compared to m-aSyn (Figure 5B).
190 Secondly, we investigated the effects of the human/mouse mismatch at position 87 on
191 fibrillization rates, based on the premise that residue 87 is in the central hydrophobic region, and
192 substitutions or deletions in this region have been shown to modulate aSyn self-assembly (7,
193 31). In contrast to our observation that substitutions at position 87 had no impact on aSyn
194 neurotoxicity in primary midbrain cultures (Figure 2), A53T/S87N and h-aSyn Chimera/S87N
195 exhibited a reduced fibrillization lag time compared to h-aSyn A53T and h-aSyn Chimera,
196 respectively (Figure S3A, B). Moreover, m-aSyn N87S and m-aSyn Chimera/N87S formed
197 amyloid-like fibrils with a longer lag time compared to m-aSyn and m-aSyn Chimera,
198 respectively (Figure S3C, D).
199 Collectively, these results suggest that differences in neurotoxicity among the human,
200 mouse, and chimeric aSyn variants (Figures 2-4) correlate weakly with differences in
201 fibrillization rates.
202
203 **Effects of human/mouse aSyn mismatches on fibril morphology and dimensions**
204 Next, we examined the impact of human/mouse aSyn mismatches on fibril morphology
205 and dimensions based on evidence that different types of aSyn fibrils (e.g. cylindrical fibrils

206 versus flatter ribbons) can trigger different levels of neurotoxicity in cellular and animal models
207 (37). Examination of incubated samples of human, mouse, and chimeric aSyn by atomic force
208 microscopy (AFM) revealed that all of the variants formed straight, rigid, unbranched fibrils,
209 organized either as individual fibrils or in fibril bundles (Figure 6A-D). Two types of fibrils
210 ('twisted' and 'non-twisted') were detected in samples of m-aSyn and h-aSyn-Chimera, whereas
211 only non-twisted fibrils were observed in samples of h-aSyn-A53T and m-aSyn-Chimera under
212 our experimental conditions. The heights of the non-twisted fibrils ranged from ~8 to ~11 nm,
213 whereas the heights of the 'valley' and 'peak' regions of the twisted fibrils ranged from ~7 to ~9
214 nm and ~11 to ~12 nm, respectively. The average pitch of twisted fibrils formed by m-aSyn and
215 h-aSyn Chimera was 123 ± 5 nm and 91 ± 8 nm, respectively (Figure 6E,F).

216 Further analysis of the fibrils by TEM also revealed the presence of straight, rigid,
217 unbranched fibrils for all of the variants (Figure 6G-L). The fibrils had similar properties as those
218 described for previously reported aSyn amyloid-like fibrils (e.g. diameter of ~10-15 nm; apparent
219 winding of two fibrils around each other via a helical twist) (26). Similar features were also
220 observed for fibrils formed by aSyn variants with the S87N or N87S substitution. There were no
221 striking differences in fibril morphology among the different aSyn variants, except that individual
222 fibrils formed by h-aSyn-Chimera had a twisted appearance similar to that observed for this
223 variant by AFM (in contrast, twisted fibrils of m-aSyn were not observed by TEM). It is unclear
224 why different results were obtained for m-aSyn and h-aSyn Chimera via AFM versus TEM,
225 although this discrepancy can potentially be explained by the fact that (i) the variants formed
226 two different types of twisted fibrils, as implied by their different pitch values (Figure 6E,F), and
227 (ii) different types of fibrils adsorb with different efficiencies to substrates with different
228 properties such as the hydrophilic mica and hydrophobic carbon-coated grids used here for
229 AFM and TEM, respectively (38).

230 Overall, these data suggest that differences in the morphologies of aSyn fibrils formed
231 under the self-assembly conditions used in this study could potentially contribute to differences
232 in neurotoxicity among the human, mouse, and chimeric aSyn variants (Figures 2-4).
233
234 **Effects of human/mouse aSyn mismatches on membrane-induced aSyn aggregation.**
235 Based on our earlier finding that lipid-induced self-assembly plays a key role in aSyn
236 neurotoxicity (16), we hypothesized that human-to-mouse substitutions should lead to a
237 decrease in aSyn aggregation propensity at membrane surfaces. Our rationale was that
238 although aSyn aggregation is primarily driven by the central hydrophobic region (7, 11, 16),
239 modifications to the C-terminal domain have been shown to modulate aSyn self-assembly (39)
240 and aSyn-membrane interactions (40) through effects on long-range interactions.
241 As a first step, we characterized the human, mouse, and chimeric variants in terms of
242 membrane affinities, based on the premise that differences in affinity could lead to differences in
243 the variants' propensity to undergo membrane-induced aggregation (16). Recombinant h-aSyn
244 WT, h-aSyn A53T, h-aSyn Chimera, m-aSyn, and m-aSyn Chimera in a monomeric state were
245 titrated with small unilamellar vesicles (SUVs) composed of egg phosphatidylglycerol (PG) and
246 egg phosphatidylcholine (PC) (1:1 mol/mol). Analysis of the samples via far-UV CD, a method
247 used to monitor the increase in aSyn α-helical structure that results from binding of the protein
248 to phospholipids, yielded similar lipid titration curves, K_d values, and maximum α-helical
249 contents for all of the aSyn variants (Figure 7A; Table S1). These results suggested that the C-
250 terminal human/mouse mismatches have little effect on the affinity of aSyn for phospholipid
251 membranes, or on the degree of α-helical structure adopted by the protein in the presence of
252 saturating lipid.
253 Next, we compared the human, mouse, and chimeric aSyn variants in terms of their
254 ability to undergo membrane-induced aggregation using a lipid-flotation assay. The proteins
255 were incubated with PG:PC SUVs under conditions that promote aSyn self-assembly, and the

256 membrane fraction was isolated by gradient centrifugation and analyzed via Western blotting.
257 The lane loaded with h-aSyn WT contained immunoreactive bands at ~45 and 60 kDa, whereas
258 the lane containing h-aSyn A53T or m-aSyn Chimera displayed more extensive laddering,
259 including bands at 75 and 100 kDa, and an intense smear of aSyn immunoreactivity in the
260 region of the gel above 245 kDa (Figure 7B). In contrast, high molecular-weight species were
261 markedly less abundant in the lanes loaded with h-aSyn Chimera or m-aSyn. Densitometry
262 analysis revealed a ~2-fold greater ratio of total oligomer band intensity to monomer band
263 intensity in the h-aSyn A53T and m-aSyn Chimera samples compared to the h-aSyn Chimera
264 and m-aSyn samples, respectively (Figure 7B). Although the results revealed a trend towards
265 an increase in the oligomer/monomer ratios for h-aSyn A53T and m-aSyn Chimera compared to
266 the human WT protein, these effects did not reach statistical significance. Collectively, these
267 data suggested that the human-to-mouse substitutions at positions 121 and 122 interfere with
268 membrane-induced aSyn aggregation.
269
270 **Effects of human/mouse aSyn mismatches on a-Syn-mediated membrane disruption.**
271 A number of groups have reported that aSyn aggregation at the membrane can affect
272 bilayer integrity via a mechanism involving phospholipid extraction coupled with aggregate
273 growth (19, 21). Recently, we found that two familial aSyn mutants with a high propensity to
274 form oligomers at membrane surfaces (A30P and G51D) (16) efficiently triggered vesicle
275 disruption under incubation conditions suitable for membrane-induced aggregation, whereas a
276 variant with a low propensity to undergo self-assembly at the membrane (A29E) exhibited no
277 vesicle permeabilization activity (22). Thus, we hypothesized that h-aSyn A53T and m-aSyn
278 Chimera should elicit greater membrane disruption than h-aSyn Chimera and m-aSyn, based on
279 the relative propensities of these variants to undergo membrane-induced aggregation (Figure
280 7B). To examine this hypothesis, we compared the human, mouse, and chimeric aSyn variants
281 in terms of their ability to disrupt vesicles using a dye release assay. PG-PC SUVs pre-loaded

282 with the fluorescent dye calcein at a concentration leading to self-quenching were incubated
283 with the aSyn variants in monomer form at 37 °C. Membrane permeabilization was assessed by
284 monitoring the increase in fluorescence intensity resulting from dequenching of the dye after its
285 release from the vesicles and dilution in the surrounding buffer. Upon extended incubation, all of
286 the aSyn-SUV mixtures displayed a time-dependent increase in fluorescence, in contrast to the
287 control sample consisting of vesicles without protein (Figure 7C). After 120 h, the fluorescence
288 emission observed for h-aSyn A53T and m-aSyn Chimera (corresponding to a yield of ~55% of
289 the maximal signal obtained by lysing the vesicles with detergent) was 2.5- and 1.5-fold greater
290 than that observed for h-aSyn Chimera and m-aSyn, respectively (Figure 7C). H-aSyn WT
291 produced a similar increase in fluorescence compared to h-aSyn A53T and m-aSyn Chimera.
292 Together, these data suggested that the human-to-mouse substitutions at positions 121 and
293 122 interfere with aSyn-mediated vesicle disruption under conditions compatible with aSyn
294 aggregation at the membrane surface.
295

296 ## Discussion

297 Understanding how human and mouse aSyn differ in terms of pathobiology is a high priority in
298 the synucleinopathy field not only because of the A/T mismatch at position 53 relevant to familial
299 PD, but also because of the widespread use of genetically engineered mice to investigate
300 molecular underpinnings of aSyn neuropathology *in vivo*. Previously, it was reported that
301 transgenic mice expressing m-aSyn downstream of the Thy-1 promoter show evidence at post-
302 mortem examination of extranigral aSyn accumulations similar to those observed in mice
303 expressing WT or mutant forms of h-aSyn (41). Moreover, Lashuel and colleagues (42) showed
304 that endogenous m-aSyn interferes with the formation of Lewy-like inclusions by h-aSyn WT in
305 cultured neurons and in mouse brain. Here we report that m-aSyn has a reduced propensity to
306 elicit dopaminergic cell death compared to h-aSyn A53T in primary midbrain cultures and

307 exhibits a similar effect when expressed from an AAV vector in rat SN. Furthermore, we show
308 for the first time that this differential toxicity is associated with differences in aSyn-mediated
309 vesicle disruption and aggregation at the membrane surface, rather than differences in aSyn
310 fibrillization previously suggested to be important for modulating its toxicity (43). Most
311 importantly, we provide evidence that these characteristics of the overtly toxic h-aSyn A53T
312 variant can be blunted, down to the same level of m-aSyn, by modification of only 2 amino acid
313 residues in positions 121 and 122 of the protein.

314 Our findings are consistent with the idea that m-aSyn has a reduced propensity to elicit
315 neurotoxicity compared to h-aSyn A53T as a result of attenuation of the toxic effects of
316 threonine 53 in the mouse protein by variations in other sites of the protein. Moreover, these
317 results support the hypothesis that mice show no signs of neurodegeneration despite
318 expressing an aSyn variant with a threonine residue at position 53 at least in part because m-
319 aSyn is intrinsically less toxic than h-aSyn A53T. The lack of nigral degeneration in mouse
320 models with altered expression of proteins that interact functionally with aSyn, including
321 transgenic mice over-expressing LRRK2 (44) and DJ-1 knockout mice (45), could also
322 potentially be explained by the reduced neurotoxicity of endogenous m-aSyn. Nevertheless,
323 despite its lower intrinsic toxicity, m-aSyn can also contribute to dopaminergic cell death in other
324 models relevant to nigral degeneration, including mice treated with MPTP (46). In addition to the
325 intrinsic biochemical differences between h-aSyn A53T and m-aSyn reported here, other factors
326 including differences in neurochemistry between the nigrostriatal systems of mice and humans
327 (47, 48) could also account at least in part for the apparent absence of early-onset aSyn
328 neuropathology in mice in contrast to human A53T patients.

329 Our data are in line with previous results showing that rat aSyn, identical to m-aSyn
330 except for a single G-to-S mismatch at position 121, triggers less extensive nigral degeneration
331 compared to h-aSyn WT, h-aSyn A30P, or h-aSyn A53T when expressed from a lentiviral vector
332 in rat midbrain (28). Moreover, we observed that rat aSyn has a similar blunted response of

333 nigral dopaminergic cell death compared to mouse aSyn in the rAAV-mediated overexpression
334 model in the rat (29). Another group reported evidence of TH^+ neuron loss and an accumulation
335 of Lewy-like inclusions in the SN of rats injected intrastriatally with preformed fibrils (PFFs)
336 prepared from recombinant m-aSyn (49). A similar but less pronounced neuropathological
337 phenotype was observed upon injecting a sample of non-fibrillized m-aSyn in rat midbrain,
338 although the interpretation of the results was complicated by uncertainty about the degree of
339 aSyn oligomerization in the injected, non-fibrillar protein sample.

340 A key finding of this study was the observation in both primary mesencephalic cultures
341 and rat midbrain that (i) h-aSyn Chimera, a variant of h-aSyn A53T with m-aSyn residues
342 introduced at positions 121 and 122, was less neurotoxic than h-aSyn A53T; and (ii) m-aSyn
343 Chimera, a variant of m-aSyn with human aSyn residues introduced at positions 121 and 122,
344 was more neurotoxic than the mouse protein. From these results, we infer that the presence of
345 glycine and serine residues at positions 121 and 122 of m-aSyn (respectively) is largely
346 responsible for offsetting the expected neurotoxic effects of threonine 53 in the murine
347 sequence. In turn, these findings reveal for the first time that residues 121 and 122 play a key
348 role in modulating aSyn-mediated neurodegeneration. Notably, in contrast to the striking effects
349 of human/mouse substitutions at positions 121 and 122, the S87N or N87S substitution had no
350 impact on the ability of human, mouse, or chimeric aSyn variants to trigger dopaminergic cell
351 death in primary midbrain cultures, suggesting that the variations in the two C-terminal residues
352 are unique in their impact on the toxicity. In support of these findings, a number of groups have
353 shown that modifications in the C-terminal domain, including truncation (31, 34) and Y125
354 phosphorylation (32), affect aSyn neurotoxicity in cellular and animal models.

355 Previously, m-aSyn was shown to form amyloid-like fibrils with a reduced lag time and a
356 greater elongation rate compared to h-aSyn WT or h-aSyn A53T (25, 26). Here we confirmed
357 these earlier findings and found that two chimeric variants, h-aSyn Chimera and m-aSyn
358 Chimera, undergo less rapid fibrillization than the mouse protein. These results indicate that the

359 human-to-mouse substitutions at positions 121 and 122 are necessary but not sufficient for the
360 enhanced fibrillization rate of m-aSyn relative to h-aSyn A53T. Because the human-to-mouse
361 and mouse-to-human substitutions at positions 121 and 122 do not have opposite effects on the
362 rate of aSyn fibrillization, we infer that the impact of each of these substitutions on aSyn self-
363 assembly is dependent on the sequence context, potentially because residues 121 and 122 are
364 involved in long-range intramolecular interactions that influence the rate of aSyn self-assembly
365 (8, 9). Additional data revealed that variants of h-aSyn A53T and h-aSyn Chimera with the S87N
366 substitution form fibrils with a decreased lag time, consistent with previously reported effects of
367 this mutation (25), whereas variants of m-aSyn and m-aSyn Chimera with the N87S substitution
368 form fibrils with an increased lag time.

369 Importantly, however, differences in fibrillization rates among the human, mouse, and
370 chimeric aSyn variants correlate only weakly with differences in neurotoxicity. For example, h-
371 aSyn A53T, h-aSyn Chimera, m-aSyn, and m-aSyn Chimera exhibit the following order of
372 fibrillization rates:

373

374 m-aSyn ≥ m-aSyn Chimera > h-aSyn A53T > h-aSyn Chimera

375

376 In contrast, the same variants exhibit the following order of neurotoxicity:

377

378 h-aSyn A53T ≈ m-aSyn Chimera > m-aSyn ≈ h-aSyn Chimera

379

380 Moreover, despite causing changes in aSyn fibrillization lag times, the S87N and N87S
381 substitutions have no impact on aSyn neurotoxicity in primary midbrain cultures, further
382 highlighting the weak correlation between fibrillization propensity and aSyn-mediated
383 neurodegeneration revealed by our study. The lack of a tight correlation may reflect the fact that
384 in mammalian cells non-membrane-bound aSyn adopts a compact disordered conformation that

385 is apparently incompatible with efficient fibrillization (5). Thus, a perturbation that favors or
386 hinders fibril formation by recombinant, natively unfolded aSyn in solution may have a very
387 different effect on the protein's conversion to neurotoxic species in its native intracellular
388 environment.

389 AFM and TEM analyses revealed that human, mouse, and chimeric aSyn formed
390 amyloid-like fibrils with different morphologies under the experimental conditions used here.
391 Namely, m-aSyn and h-aSyn Chimera, the two variants with reduced neurotoxicity, formed both
392 twisted and non-twisted fibrils, whereas only non-twisted fibrils were formed by h-aSyn A53T
393 and m-aSyn Chimera. These results are consistent with solid-state NMR data showing that
394 fibrils formed by h-aSyn WT and m-aSyn differ in terms of protofilament substructure (50, 51),
395 although previous EM analyses revealed no major morphological differences between fibrils
396 prepared from human A53T and mouse aSyn (25, 52). Multiple groups have shown that
397 injecting PFFs into the brains of WT or transgenic rodents initiates the aggregation of
398 endogenous aSyn via a seeding mechanism, leading to the formation of Lewy-like inclusions
399 (49, 53, 54). Moreover, evidence suggests that different types of fibrils (e.g. cylindrical fibrils
400 versus ribbons distinguishable by EM) can act as prion-like 'strains' with different abilities to
401 undergo cell-to-cell transmission throughout the brain (37). Our AFM and TEM data imply that
402 m-aSyn and h-aSyn Chimera could potentially form different fibrillar strains (characterized by
403 increased amounts of twisted fibrils) compared to the other aSyn variants, and, therefore, the
404 differences in *in vivo* neurotoxicity reported here could be due to differences in the variants'
405 abilities to seed aSyn neuropathology in rat brain. However, this interpretation is challenged by
406 evidence that (i) h-aSyn A53T can form twisted fibrils under certain incubation conditions (55);
407 and (ii) PFFs formed from recombinant m-aSyn induce inclusion formation and dopaminergic
408 cell death with greater or similar efficiency (respectively) compared to h-aSyn A53T PFFs
409 following their injection in mouse SN (56), in contrast to the reduced neurotoxicity of m-aSyn
410 compared to h-aSyn A53T reported here. Additional studies are needed to assess whether

411 human, mouse, or chimeric aSyn variants produce different fibrillar strains with different levels of
412 neurotoxicity *in vivo*.

413 Previously we reported that two familial substitutions, A30P and G51D, increase aSyn
414 neurotoxicity by enhancing the protein's ability to form aggregates at membrane surfaces (16).
415 Here we show that two aSyn variants with a higher propensity to elicit dopaminergic cell death
416 in primary culture and *in vivo*, h-aSyn A53T and m-aSyn Chimera, undergo membrane-induced
417 self-assembly with greater efficiency compared to two variants with lower neurotoxicity, h-aSyn
418 Chimera and m-aSyn. These results suggest that mouse-to-human substitutions at positions
419 121 and 122 cause an increase in aSyn neurotoxicity by promoting Syn aggregation at
420 membrane surfaces, whereas human-to-mouse substitutions have the opposite effect. Because
421 all of the aSyn variants examined in this study exhibited similar affinities for PG:PC SUVs, we
422 infer that human-to-mouse substitutions interfere with lipid-induced aSyn aggregation not by
423 favoring binding of the central hydrophobic domain to the membrane, but rather by inducing a
424 conformational change in the C-terminal region that disrupts aSyn self-assembly, potentially via
425 perturbation of long-range interactions (8, 9, 40). Consistent with this scenario, data from
426 several studies suggest that modifications in the C-terminal region (namely, Y125
427 phosphorylation or nitration, or the nitration of all three C-terminal tyrosine residues) can
428 modulate the conformation of the N-terminal and central hydrophobic domains of the
429 membrane-bound form of the protein (40, 57, 58). These findings support the idea that long-
430 range interactions can occur in the membrane-associated form of aSyn, in turn suggesting that
431 the human-to-mouse substitutions at positions 121 and 122 could potentially influence
432 membrane-induced aSyn aggregation by altering these intramolecular contacts. Moreover,
433 Burré et al. (59) have proposed a model wherein oligomers formed by aSyn at the membrane
434 surface consist of neighboring aSyn molecules with their C-terminal alpha-helices arranged in
435 an anti-parallel configuration. In this arrangement, the aspartate residue at position 121 of
436 human aSyn could potentially participate in electrostatic interactions with positively charged

437 residues on a neighboring subunit, and in turn these interactions could favor the formation of
438 pathological aSyn aggregates at the membrane surface. This idea is also supported by
439 computational data from our group suggesting that intermolecular interactions between the C-
440 terminal domain and central hydrophobic region play a key role in aSyn dimerization at the
441 surface of anionic phospholipid membranes (60).

442 In the current study and in our earlier work (16, 22), SDS-resistant aSyn oligomers were
443 detected in the lipid fraction of protein/SUV mixtures isolated by lipid flotation. These data
444 indicate that membrane-bound aSyn oligomers were generated upon incubating the protein with
445 SUVs. The formation of these membrane-bound oligomers could occur as a result of (i) aSyn
446 aggregation at the membrane surface, or (ii) aSyn aggregation in solution, followed by the
447 binding of the aggregates to the membrane. Three observations argue against the second
448 scenario. First, we find that aSyn does not form aggregates when incubated in the absence of
449 SUVs under the same conditions as those used in the membrane-induced aggregation assay.
450 Second, the relative rates at which aSyn variants form oligomers in the presence of SUVs
451 correlate poorly with the relative rates at which the variants undergo self-assembly in the
452 absence of phospholipids (16). Third, we recently showed that ENSA, a protein that interacts
453 selectively with membrane-bound aSyn (61), inhibits aSyn aggregation in the presence of
454 SUVs, whereas it does not interfere with aSyn fibrillization in the absence of lipids (22). The fact
455 that ENSA does not inhibit aSyn fibril formation in the absence of SUVs suggests that the
456 inhibitory effect of ENSA on aSyn self-assembly in the presence of lipids must arise from its
457 interaction with aSyn at the membrane surface. In turn, this evidence supports the idea that
458 aSyn forms oligomers on the membrane when incubated with SUVs under the conditions
459 described here.

460 Importantly, our data reveal a strong correlation between aggregation propensity at
461 membrane surfaces and neurotoxicity among the human, mouse, and chimeric aSyn variants,
462 and thus they further support the hypothesis that lipid-induced self-assembly plays a key role in

463 aSyn-mediated neurodegeneration (11, 16, 18, 22). The importance of membrane-induced aSyn
464 aggregation to the pathogenesis of synucleinopathy disorders is further underscored by
465 evidence that non-membrane-associated aSyn adopts a compact, aggregation-resistant
466 conformation, with little exposure of the central hydrophobic region, in mammalian cells (5).
467 Although it is uncertain why all of the aSyn variants examined here formed PK-resistant
468 aggregates in rat striatum, one explanation could be that the inclusions consist of fibrils derived
469 from both membrane-bound and non-membrane-bound forms of aSyn (20, 21). Accordingly, a
470 decrease in the levels of fibrils formed in the presence of lipids could be offset by an increase in
471 the levels of fibrils formed away from the membrane in the case of m-aSyn, whereas the
472 opposite scenario could be true in the case of h-aSyn A53T. Consistent with this idea, data
473 reported by multiple groups imply that aSyn can undergo various forms of self-assembly,
474 leading to the formation of different types of aggregated species with different degrees of
475 neurotoxicity, in cell culture models, aSyn transgenic mice, and the brains of synucleinopathy
476 patients (62-66). Although our results highlight the importance of membrane-induced aSyn
477 aggregation to aSyn-mediated dopaminergic cell death, we suggest that aSyn aggregates
478 formed both at membrane surfaces and in solution likely contribute to the overall
479 neuropathology of synucleinopathy disorders. Assessing whether differences in the rates or
480 extents of aSyn oligomerization in the absence of membranes also account at least in part for
481 differences in neurotoxicity among the aSyn variants is an important goal for future studies.
482 A final key outcome of this study was our finding that the relatively neurotoxic variants h-
483 aSyn A53T and m-aSyn Chimera elicit the disruption of synthetic vesicles under conditions
484 favoring membrane-induced aSyn aggregation with greater efficiency than the less toxic
485 variants h-aSyn Chimera and m-aSyn. These data suggest that mouse-to-human substitutions
486 at positions 121 and 122 enhance aSyn neurotoxicity by promoting aSyn-mediated membrane
487 permeabilization, whereas human-to-mouse substitutions have the opposite effect.
488 Unexpectedly, we found that h-aSyn WT triggered vesicle disruption to a similar extent as h-

489 aSyn A53T and m-aSyn Chimera. This observation was inconsistent with the fact that h-aSyn
490 WT exhibited a non-significant trend towards less extensive membrane-induced self-assembly,
491 or with evidence from our earlier studies that h-aSyn WT is considerably less toxic than h-aSyn
492 A53T in primary midbrain cultures (16) and causes neurodegeneration less rapidly than h-aSyn
493 A53T in rat midbrain (67). As one possibility, the current findings can be interpreted to mean
494 that h-aSyn WT engages in different molecular interactions during aggregation at the membrane
495 surface compared to h-aSyn A53T or m-aSyn Chimera, resulting in an increase in the extent of
496 membrane permeabilization relative to the total amount of aggregate formed. Consistent with
497 this idea, evidence from multiple studies suggests that h-aSyn WT and familial aSyn mutants
498 can form different types of amyloid-like fibrils (68-70). Overall, our data reveal a strong
499 correlation between vesicle disruption and neurotoxicity among the human, mouse, and
500 chimeric aSyn variants, and thus they support the notion that membrane permeabilization
501 associated with lipid-induced self-assembly plays a key role in aSyn-mediated
502 neurodegeneration. These findings are consistent with evidence that h-aSyn E57K, a variant
503 with a high propensity to form aggregates on a supported lipid bilayer and elicit membrane
504 damage, causes extensive dopaminergic cell death when expressed in rat SN (19, 35).
505 Previous findings reported by Volles et al. (71, 72) suggest that aSyn oligomers formed
506 in the absence of membranes fail to permeabilize low-diameter vesicles composed of a mixture
507 of anionic and zwitterionic lipids. Accordingly, we infer that the vesicle disruption observed in
508 aSyn-SUV mixtures in this study and in our earlier work (22) results from aSyn self-assembly at
509 the membrane surface. These observations further corroborate the idea that aSyn forms
510 oligomers on the membrane when incubated with SUVs under the conditions described in this
511 study. Moreover, oligomeric m-aSyn prepared in the absence of membranes was reported by
512 Volles et al. (71) to permeabilize vesicles composed of anionic lipids with a similar efficiency
513 compared to oligomeric h-aSyn A53T, contrary to the difference in the variants' neurotoxicity
514 reported here. This observation suggests that vesicle disruption associated with lipid-induced

515 aSyn aggregation plays a more important role than membrane permeabilization by preformed
516 oligomers in aSyn-mediated neurodegeneration *in vivo*.
517
518 **Conclusions** We report for the first time that m-aSyn has a reduced ability to elicit
519 dopaminergic cell death compared to h-aSyn A53T in primary mesencephalic cultures and in rat
520 midbrain. Our results highlight the central importance of membrane-induced aSyn aggregation
521 and vesicle disruption in aSyn neurotoxicity, and they reveal a C-terminal sequence motif
522 encompassing residues 121 and 122 with an important role in modulating these activities.
523 Collectively, these findings provide a strong rationale for developing therapies aimed at
524 inhibiting aSyn aggregation at membrane surfaces, including interventions that target the C-
525 terminal domain, as a strategy to slow neurodegeneration in the brains of synucleinopathy
526 patients (16, 18, 22).
527

528 Experimental Procedures

529 **Materials.** Unless otherwise stated all chemicals were purchased from Sigma-Aldrich (St. Louis,
530 MO or Stockholm, Sweden). DMEM, FBS, penicillin-streptomycin, Lipofectamine 2000,
531 Optimem, Trypsin-EDTA, ProLong Gold Antifade Reagent with DAPI, Proteinase K (25530-
532 049), and the Virapower Adenoviral Expression System were obtained from Invitrogen
533 (Carlsbad, CA). RPMI medium, phenol red-free RPMI medium, Nuserum, Plus slides
534 (J3800AMNZ), Phosphatase Inhibitor Mini Tablets, bicinchoninic acid (BCA) assay reagents,
535 Coomassie Brilliant Blue, and the Immobilon-FL PVDF membrane was purchased from Thermo
536 Fisher Scientific (Rockford, IL). The QuickTiter Adenovirus Titer Elisa kit was purchased from
537 Cell Biolabs (San Diego, CA). Antisedan, Temgesic, and the Fentanyl/Dormitor mixture were
538 obtained from Apoteksbolaget, (Stockholm, Sweden). The Vectastain ABC kit was purchased
539 from Vector Laboratories, Inc. (Burlingame, CA), and 3,3'-diaminobenzidine (DAB Safe) was

540 obtained from Saveen Werner (Limhamnsvägen, Sweden). Isopropyl β-D-1-
541 thiogalactopyranoside, ampicillin, and PMSF were purchased from Gold Biotechnology (St.
542 Louis, MO). Recombinant Syk, Src, and Fyn kinases were obtained from SignalChem
543 (Richmond, BC, Canada). L-α-phosphatidylcholine (egg PC), L-α-phosphatidylglycerol (egg
544 PG), and phospholipid extrusion membranes were purchased from Avanti Polar Lipids
545 (Alabaster, AL). Iodixanol and the enhanced chemifluorescence (ECF) substrate were obtained
546 from GE Life Sciences (Pittsburgh, PA). The nitrocellulose membrane was purchased from Bio-
547 Rad Laboratories (Hercules, CA). 100 kDa spin filters and 10 kDa concentration filters were
548 obtained from Millipore (Billerica, MA or Solna, Sweden). SH-SY5Y cells were purchased from
549 ATCC (Manassas, VA) (catalog # CRL-2266, RRID:CVCL_0019), and the PC12 Tet-Off cell line
550 (RRID:CVCL_V361) was obtained from Clontech Laboratories (Mountain View, CA). Cell line
551 authentication and mycoplasma testing were carried out by IDEXX BioResearch (Columbia,
552 MO) (cell line identities were confirmed via species-specific PCR evaluation and STR profiling,
553 and both cell lines were shown to be mycoplasma negative). A plasmid encoding murine Syk
554 fused at its C-terminus with EGFP (Syk-GFP) (73) was provided by Dr. Robert Geahlen (Purdue
555 University), and vectors encoding human GST-Src and GST-Fyn (74) were provided by Dr.
556 Laurie Parker (University of Minnesota), with permission from Dr. Benjamin Turk (Yale
557 University).
558
559 **Antibodies.** The following antibodies were used in these studies:
560 Primary cell culture – chicken anti-MAP2 (CPCA-MAP2, RRID:AB_2138173, EnCor
561 Biotechnology, Gainesville, FL); rabbit anti-tyrosine hydroxylase (TH) (AB152,
562 RRID:AB_390204, Millipore, Bellerica, MA); anti-rabbit IgG-Alexa Fluor 488 (R37116,
563 RRID:AB_2556544) and anti-chicken IgG-Alexa Fluor 594 (A11042, RRID:AB_142803)
564 (Thermo Fisher Scientific, Rockford, IL).

565 *In vivo* experiments – human-specific syn211 (36-008, RRID:AB_310817, Millipore,
566 Germany); mouse anti-aSyn, clone 42 (Syn-1) (610787, RRID:AB_398108, BD Biosciences,
567 UK); rabbit anti-TH (P40101-0, RRID:AB_461064**,** Pel-freeze, USA); rabbit anti-VMAT2
568 (ab81855, RRID:AB_2188123*,* Abcam, UK or 20042, RRID:AB_10013884*,* Immunostar, USA);
569 mouse anti-HuC/HuD, clone 16A11 (A21271, RRID:AB_221448*,* Thermo Scientific, USA);
570 biotinylated secondary antibodies (Vector Laboratories Inc., USA).
571 Western blotting – mouse anti-aSyn, clone 42 (Syn-1) (610787, RRID:AB_398108, BD
572 Biosciences, San Jose, CA); mouse anti-phosphotyrosine, clone 27B10 (APY03-HRP,
573 Cytoskeleton, Denver, CO); rabbit anti-pY125-aSyn (ab131466, RRID:AB_11158765, Abcam,
574 Cambridge, MA, or A1219, BioVision, Milpitas, CA); mouse anti-β-actin, clone AC-74 (A5316,
575 RRID:AB_476743, Sigma-Aldrich); mouse anti-GFP, clone B-2 (sc-9996, RRID:AB_627695,
576 Santa Cruz Biotechnology, Dallas, TX); rabbit anti-Src (2108, RRID:AB_331137), rabbit anti-Fyn
577 (4023, RRID:AB_2108441), AP-linked anti-mouse IgG (7056, RRID:AB_330921), and AP-linked
578 anti-rabbit IgG (7054, RRID:AB_2099235) (Cell Signaling Technology, Danvers, MA); goat anti-
579 mouse IR-Dye 680RD (92568070, RRID:AB_2651128) and goat anti-rabbit IR-Dye 800CW
580 (92532211, RRID:AB_2651127) (Li-COR, Lincoln, NE).
581
582 **Preparation of bacterial expression constructs.** Bacterial expression constructs encoding h-
583 aSyn WT (pT7-7-h-aSyn), h-aSyn A53T (pT7-7-h-aSyn-A53T), and m-aSyn (pT7-7-m-aSyn)
584 were described previously (26). A construct encoding h-aSyn Chimera was generated by
585 replacing the BamHI-HindIII fragment of pT7-7-h-aSyn-A53T (encompassing base pairs 354-
586 423 of the h-aSyn A53T cDNA) with the equivalent fragment from pT7-7-m-aSyn. A construct
587 encoding m-aSyn Chimera was generated by replacing the BamHI-HindIII fragment of pT7-7-m-
588 aSyn (encompassing base pairs 354-423 of the m-aSyn cDNA) with the equivalent fragment
589 from pT7-7-h-aSyn-A53T. pT7-7 constructs encoding A53T/D121G, A53T/N122S, A53T/S87N,

590 h-aSyn Chimera S87N, m-aSyn N87S, and m-aSyn Chimera N87S were generated via site-
591 directed mutagenesis using the QuikChange method (Stratagene). The sequence of the DNA
592 insert in each bacterial expression construct was verified using an Applied Biosystems
593 (ABI3700) DNA sequencer (Purdue Genomics Core Facility).
594
595 **Adenoviral vector design and virus production.** Adenoviral constructs encoding h-aSyn WT
596 and h-aSyn A53T were described previously (16, 75). cDNAs encoding h-aSyn Chimera,
597 A53T/D121G, A53T/N122S, A53T/S87N, and h-aSyn Chimera S87N (obtained using the pT7-7
598 constructs outlined above as PCR templates) were subcloned as KpnI-XhoI fragments into the
599 entry vector pENTR1A. cDNAs encoding m-aSyn, m-aSyn Chimera, and m-aSyn Chimera
600 N87S were subcloned as SalI-XhoI fragments into pENTR1A. Inserts from the pENTR1A
601 constructs were then transferred into the pAd/CMV/V5 adenoviral expression vector via
602 recombination using Gateway LR Clonase. The sequence of the DNA insert in each adenoviral
603 construct was verified using an Applied Biosystems (ABI3700) DNA sequencer (Purdue
604 Genomics Core Facility). Adenoviral constructs were packaged into virus via lipid-mediated
605 transient transfection of the HEK 293A packaging cell line. Purified adenoviral particles were
606 titered using the QuickTiter Adenovirus Titer Elisa kit.
607
608 **AAV vector design and virus production.** Adeno-associated viral vectors of serotype 5
609 (AAV5) were comprised of a genome cassette flanked by inverted terminal repeats (ITR2). The
610 cassette contained a chicken beta-actin promoter in combination with a CMV enhancer element
611 (CBA) leading to expression of one of the four different transgenes. Genes were PCR-amplified
612 with the plasmids pENTR1A h-aSyn A53T, pENTR1A h-aSyn Chimera, pENTR1A m-aSyn, and
613 pENTR1A m-aSyn Chimera as templates and subcloned as HindIII-SpeI fragments in the pTR-
614 UF20 plasmid. The validity of the constructs was confirmed by restriction analysis and Sanger
615 sequencing. Downstream of each cDNA insert was an h-SV40 polyA transcription termination

616 sequence. HEK293 cells were co-transfected at a confluency of 70-80% using the calcium-
617 phosphate precipitation method. Plasmids used here encode essential adenoviral packaging
618 and AAV5 capsid genes as previously described (76). Three days after transfection, cells were
619 harvested in PBS and lysed by performing three freeze-thaw cycles in a dry ice/ethanol bath.
620 The lysate was then treated with benzonase and purified using a discontinuous iodixanol
621 gradient followed by Sepharose Q column chromatography (77). Vectors were concentrated
622 using a 100 kDa molecular weight cut-off column, and titers of the stock solution were
623 determined by qPCR using primers and probes targeting the ITR sequence. Before being used
624 in an experiment, vectors were diluted in PBS, pH 7.4 and re-titered, yielding the values
625 reported in the Results and in Figure 3.
626
627 **Preparation and treatment of primary mesencephalic cultures.** Primary midbrain cultures
628 were prepared via dissection of day 17 embryos obtained from pregnant Sprague-Dawley rats
629 (Harlan, Indianapolis, IN, USA) as described (16, 75). All of the procedures involving animal
630 handling were approved by the Purdue Animal Care and Use Committee. The cells were plated
631 on poly-L-lysine-treated 48-well plates at a density of 163,500 cells per well. Five days after
632 plating, the cells were treated with cytosine arabinofuranoside (AraC) (20 μM, 48 h) to inhibit the
633 growth of glial cells. At this stage (i.e., 7 days in vitro (DIV)), the neurons appeared differentiated
634 with extended processes. The cultures were transduced with adenoviruses encoding the aSyn
635 variants for 72 h at a multiplicity of infection (MOI) ranging from 7 to 15 to ensure equal
636 expression levels as determined via Western blotting. After incubation for an additional 24 h in
637 fresh medium without virus, the cells were fixed in 4% (w/v) PFA in PBS (pH 7.4). The cells
638 were then washed in PBS and incubated with chicken anti-MAP2 (1:2000) and rabbit anti-
639 tyrosine hydroxylase (TH) 1:500) for 24 h. After an additional wash in PBS, the cultures were
640 incubated with AlexaFluor 594-conjugated goat anti-chicken and AlexaFluor 488-conjugated

641 goat anti-rabbit secondary antibodies (1:1000) for 1 h at 22 °C. ProLong Gold Antifade Reagent
642 with DAPI was applied to each well, and a coverslip was added.
643
644 **Measurement of neuronal viability in midbrain cultures.** Relative dopaminergic cell viability
645 was evaluated as described (16, 75). $MAP2^+$ and TH^+ cells were counted in a blinded manner in
646 at least 10 randomly chosen observational fields (approximately 500-1000 neurons total) for
647 each experimental condition using a Nikon TE2000-U inverted fluorescence microscope (Nikon
648 Instruments, Melville, NY) equipped with a 20x objective. The data are expressed as the
649 percentage of $MAP2^+$ neurons that are also TH^+ to correct for variation in cell density. Each
650 experiment was repeated a minimum of 3 times with cultures isolated from different pregnant
651 rats.
652
653 **Animals for in vivo experiments.** Young adult Sprague-Dawley rats received from Charles
654 River (Kisslegg, Germany) were housed on a 12 h light-dark cycle with *ad libitum* access to
655 water and food. All experimental procedures were approved by the Ethical Committee for Use of
656 Laboratory Animals in the Lund-Malmö region.
657
658 **Stereotaxic surgery.** Rats were anesthetized via i.p. injection of a 20:1 mixture of Fentanyl and
659 Dormitor (6 mL/kg). After placing each animal into a stereotaxic frame (Stoelting, Wood Dale,
660 USA), the SN was targeted unilaterally using the following coordinates: anteroposterior (AP), -
661 5.0 mm; mediolateral (ML), -2.0 mm from bregma; and dorsoventral (DV), -7.2 mm from the
662 dura. The tooth bar was adjusted to -2.3 mm. A pulled glass capillary (about 60-80 μm in
663 diameter) was attached to a 5 μL Hamilton syringe equipped with a 22s gauge needle and used
664 to deliver 2 μL of rAAV5 vector solution at a pulsed injection of 0.1 μL every 15 sec. After
665 delivery of the vector, the capillary was left in place for 5 min, retracted 0.1 mm, and after 1 min

666 it was slowly removed from the brain. After closing the wound with clips, Antisedan and
667 Temgesic were administered s.c. as an analgesic treatment and to reverse the anesthesia.
668
669 **Histology.** An overdose of sodium pentobarbital was used to kill rats 8 weeks after vector
670 delivery. Animals were perfused via the ascending aorta first with 50 mL of 0.9% (w/v) NaCl
671 followed by 250 mL of ice-cold 4% (w/v) PFA in 0.1 M phosphate buffer, pH 7.4, for 5 min.
672 Brains were taken out and post-fixed in 4% (w/v) PFA for 24 h and then incubated in 25% (w/v)
673 sucrose for cryoprotection. Brains were cut on a microtome (Microm HM450, Thermo Scientific,
674 USA) in 35 µm-thick coronal sections and placed into antifreeze solution (0.5 M phosphate
675 buffer, 30% (v/v) glycerol, 30% (v/v) ethylene glycol) at -20 °C for long term storage until further
676 processed.
677 Immunohistochemical staining was performed on free-floating brain sections. Specimens
678 were rinsed with Tris-buffered saline (TBS) buffer (5 mM Tris-HCl, 15 mM NaCl, pH 7.6). Only
679 TH staining required an antigen retrieval step carried out for 30 min at 80 °C using Tris/EDTA
680 buffer (10 mM Tris-HCl, 1 mM EDTA, pH 9.1). This step was terminated by repeated washes in
681 TBS at 22 °C. Endogenous peroxidase activity was quenched using a solution of 3% (v/v) H_2O_2
682 and 10% (v/v) methanol in TBS buffer for 30 min, and the reaction was stopped by washing
683 sections 3 times with TBS. To block unspecific binding sites, sections were incubated for 30 min
684 in 0.05% (v/v) Triton X-100 in TBS buffer (TBS-T) containing 5% (v/v) normal serum from the
685 same species as that in which the secondary antibody was raised. The primary antibodies were
686 then applied in 1% (w/v) BSA in TBS-T overnight at 22 °C: human-specific syn211 at 1:100,000;
687 Syn-1 at 1:10,000; TH at 1:5,000; VMAT2 ab81855 at 1:4,000, or 20042 at 1:10,000; HuC/HuD
688 1:200. The next day sections were washed in TBS-T, and the appropriate biotinylated
689 secondary antibody (1:200) was applied in 1% (w/v) BSA in TBS-T for 1 h. Specimens were
690 rinsed once more with TBS-T and further incubated in a solution containing avidin-biotin-
691 peroxidase complexes (Vectastain ABC kit, Vector Laboratories Inc., USA) for 1 h. Staining was

692 visualized using 3,3'-diaminobenzidine (DAB Safe) and 0.01% (v/v) H_2O_2. Sections were then
693 mounted on chromatin-gelatin coated glass slides, dehydrated in increasing alcohol solutions,
694 cleared with xylene, and applied to coverslips using DPX (06522, Sigma-Aldrich, Sweden).
695 For cresyl violet staining, sections were mounted on chromatin-gelatin coated glass
696 slides and dried overnight. Sections were then hydrated in decreasing alcohol solutions and
697 stained for 30 sec in 0.5% (w/v) cresyl violet + 0.1% (v/v) acetic acid. After rinsing specimens
698 with H_2O, sections were dehydrated in increasing alcohol solutions, cleared in xylene, and
699 coverslipped using DPX.
700 To visualize insoluble aggregates, sections were treated with Proteinase K. For this
701 purpose, specimens were first rinsed with potassium-containing phosphate-buffered saline
702 (KPBS) and then heat-treated at 80°C for 30 min in KPBS. Sections were then quenched using
703 3% (v/v) H_2O_2 and 10% (v/v) methanol in KPBS for 30 min. After mounting sections on plus
704 slides, the sections were incubated in a KPBS solution containing 10 µg/mL Proteinase K for
705 either 5 or 45 min. The same staining protocol was applied as described above using the aSyn-
706 specific primary antibody Syn-1 at 1:1,000.
707
708 **Stereological analysis.** In order to estimate surviving TH^+ nigral neurons, an unbiased
709 stereological quantification using the optical fractionator method (78, 79) was applied. The
710 implementation of a random starting position and systematic sampling was done using the
711 Visiopharm VIS software (version 4.5.5.433 Visiopharm A/S, Denmark) and a Nikon Eclipse 80i
712 light microscope fitted with an xy motorized stage, a motorized z-axis (Prior, UK), and a
713 microcator (Heidenheim, Germany). Through the rostro-caudal axis of the SN, every 6th section
714 was stained for TH. Regions of interest were outlined with a 4x objective, and counting was
715 executed using a 60x oil-immersion objective with a numerical aperture of 1.4. Counting
716 parameters were set to reach at least 100 cell counts per hemisphere. Estimation of the total
717 number of TH^+ cells was performed by a single blinded investigator. The coefficient of error due

718 to the sampling was calculated based on Gundersen and Jensen (80), and values lower than
719 0.1 were considered acceptable. The contralateral uninjected side of each animal served as an
720 internal control, and values were expressed as a percentage of cell counts on the injected side
721 relative to the intact side (mean ± SEM).
722
723 **Densitometry.** The optical density of TH^+ and $VMAT2^+$ fibers was measured on digital images
724 of coronal striatal sections using the Zeiss microscope (Axio Zoom.V16, Zeiss, Germany). The
725 striatum of every 24th section in the rostro-caudal axis – in total 6 sections per brain – was
726 outlined using ImageJ, and optical density readings were corrected for non-specific background
727 using density measurements from the *corpus callosum* of each animal. Data consisting of
728 means ± SEM from all brains are expressed as a percentage of contralateral side values.
729
730 **Protein purification.** Recombinant aSyn variants were purified from BL21 (DE3) cells
731 transformed with pT7-7 constructs as described (16). The final purity of each protein was found
732 to be > 98% as determined by SDS-PAGE with Coomassie Blue staining.
733
734 **aSyn fibrillization.** Lyophilized aSyn was dissolved in PBS (pH 7.4) with 0.02% [v/v] NaN_3, and
735 the solution was filtered by successive centrifugation steps through a 0.22 µm spin filter and a
736 100 kDa centrifugal filter to isolate monomeric protein. The stock solution was dialyzed against
737 the same buffer (24 h at 4 °C) to remove excess salt. Fibrillization solutions of aSyn were
738 prepared by diluting the appropriate stock solutions of dialyzed protein with buffer to a final
739 concentration of 35 µM in the wells of a 96-well plate. To determine the extent of aSyn
740 fibrillization, thioflavin T (ThioT, final concentration, 20 µM) was added to the fibrillization
741 solutions, which were incubated at 37 °C with shaking at the 'normal' setting in a Spectra Fluor
742 Plus or Genios plate reader (Tecan, Upsala, Sweden). ThioT fluorescence was measured with
743 excitation at 440 nm and emission at 490 nm. Mean ThioT fluorescence data determined from 3

744 or 4 technical replicates (defined here as samples treated identically in a single experiment)
745 were normalized using the following equation:
746

747 $$normalized\ fluorescence = \frac{F_t - F_{min}}{F_{max} - F_{min}} \quad \text{(Eq. 1)}$$

748

749 where F_t is the ThioT fluorescence emission intensity at time t, and F_{min} and F_{max} are the
750 minimum and maximum fluorescence intensities during the incubation, respectively.
751

752 **Lipid vesicle preparation.** Small unilamellar vesicles (SUVs) (diameter = 50 nm) were
753 prepared as described (16). We opted to examine SUVs composed of egg PG and egg PC (1:1
754 mol/mol) because they contain anionic lipids necessary for aSyn membrane interactions (12)
755 and this lipid composition is compatible with producing stable 50 nm vesicles (16). Egg PG and
756 egg PC suspended in chloroform were mixed in a round bottom flask. The chloroform was
757 evaporated under a nitrogen stream and further dried under vacuum for 1 h. Dried lipids were
758 suspended in PBS, and 50 nm SUVs were prepared by extruding the suspension through a
759 Whatman membrane. The size of the vesicles was confirmed by dynamic light scattering. Lipid
760 vesicles were stored at 4 °C prior to use.
761

762 **Circular dichroism.** Far-UV CD measurements were performed as described (16) using a
763 Chirascan SC spectrometer (Applied Photophysics, Leatherhead, UK). Solutions of recombinant
764 aSyn (5 μM in 20 mM KPi, pH 7.4) in the absence or presence of SUVs (protein-to-lipid ratio,
765 1:50 to 1:1600, mol/mol) were analyzed in a 1 mm quartz cuvette at 25°C. The ellipticity at 222
766 nm was recorded and background corrected to eliminate scattering signals arising from the
767 SUVs. The mean residue molar ellipticity at 222 nm ($[\theta]_{MR,222}$) was calculated using the
768 following equation:

769

770 $$[\theta]_{MR,222} = \theta_{222}/10Cnl \quad \text{(Eq. 2)}$$

771

772 where θ_{222} is the observed (background corrected) ellipticity at 222 nm in millidegrees, C is the
773 protein concentration in M, n is the number of amino acid residues in the protein, and l is the
774 path length of the cuvette in cm. Binding curves were generated by plotting $[\theta]_{MR,222}$ versus the
775 lipid concentration. Curves were analyzed by fitting to the following equation:

776

777 $$R = R_0 - (R_0 - R_f)\frac{K_d + C + L/N - \sqrt{(K_d + C + L/N)^2 - 4CL/N}}{2C} \quad \text{(Eq. 3)}$$

778

779 where *R* is the measured $[\theta]_{MR,222}$ at a given lipid concentration, R_0 is $[\theta]_{MR,222}$ in the absence
780 of lipid, R_f is $[\theta]_{MR,222}$ in the presence of saturating lipid, *L* is the total lipid concentration, *C* is
781 the total protein concentration, *Kd* is the apparent macroscopic dissociation equilibrium
782 constant, and *N* is the binding stoichiometry (lipids/protein) (16, 81).

783 To determine the maximal helical content of each aSyn variant, we used the following
784 equations:

785 $$H = 100\% \frac{(\theta - \theta_{coil})}{(\theta_\alpha - \theta_{coil})} \quad \text{(Eq. 4)}$$

786

787 $$\theta_\alpha = -40000\left(1 - \frac{2.5}{n}\right) + 100t \quad \text{(Eq. 5)}$$

788

789 $$\theta_{coil} = 640 - 45t \quad \text{(Eq. 6)}$$

790

791 where *H* is the maximal % helicity, θ is $[\theta]_{MR,222}$ in the presence of saturating lipid (R_f in Eq. 3),
792 θ_α is the $[\theta]_{MR,222}$ value of an idealized α-helical peptide, θ_{coil} is the $[\theta]_{MR,222}$ value of an

793 idealized random coil peptide, n is the number of amino acid residues in the protein (= 140), and
794 t is the temperature (25 °C) (16, 82, 83).
795
796 **Lipid flotation assay.** Lipid flotation analyses were carried out as described (16, 22).
797 Lyophilized aSyn was resuspended in PBS with 0.02% (w/v) NaN_3, and the solution was
798 dialyzed against the same buffer to remove salts and filtered by successive centrifugation steps
799 through a 0.22 µm spin filter and a 100 kDa centrifugal filter to isolate monomeric protein. aSyn
800 (40 µM) was incubated with PG:PC SUVs (protein-to-lipid ratio, 1:20 mol/mol) at 37°C for 72 h
801 in a total volume of 60 µL. After incubation, the sample was mixed with 4 mL of 30% (v/v)
802 iodixanol solution and overlaid with 7.0 mL of 25% (v/v) iodixanol and 350 µL of 5% (v/v)
803 iodixanol in a polyalomar tube (Beckman, Miami, FL). All of the above iodixanol solutions were
804 prepared in lipid flotation buffer (10 mM HEPES, pH 7.4, 150 mM NaCl). The samples were
805 spun at 200,000 x g in a Beckman SW 41 Ti rotor for 4 h. The membrane fraction was carefully
806 collected from the 5% iodixanol fraction at the top of the gradient, concentrated using a 10 kDa
807 spin filter, and analyzed via Western blotting using a primary antibody specific for aSyn (Syn-1)
808 (1:1,500) (16, 22). In general, we found that the rate of aSyn aggregation increased in the
809 presence of SUVs that had been stored for ~2-4 weeks at 4 °C (16).
810
811 **Synthetic vesicle disruption assay.** Calcein-loaded egg PG:PC SUVs were prepared as
812 described (84) with some modifications. A solution of calcein (170 mM) was prepared in H_2O
813 using NaOH to adjust the pH to 7.4. The final osmolality was 280 mOsm/kg. The calcein
814 solution was used to resuspend dried egg PG:PC lipids, and the suspension was extruded
815 through a Whatman membrane to generate 50 nm SUVs. Calcein-containing vesicles were
816 isolated from free calcein via gel filtration through a Sephadex G-50 column pre-equilibrated
817 with PBS, pH 7.4, 0.02% (w/v) NaN_3 (280 mOsm/kg). Fractions containing isolated vesicles

818 were pooled and stored at 4 °C until use. Calcein-loaded vesicles were found to be very stable,
819 with no spontaneous dye leakage observed over several weeks.

820 For membrane disruption experiments, monomeric aSyn variants were isolated as
821 described above (see 'Lipid Flotation Assay'). Each aSyn variant (40 μM) was incubated with
822 calcein-loaded PG:PC SUVs (protein-to-lipid ratio, 1:20 mol/mol) at 37°C in a total volume of 40
823 μL. At each time point, 3 μL of the reaction mixture was diluted into 180 μL of PBS, and the
824 diluted samples were analyzed with a Fluoromax-3 spectrofluorometer (Horiba Scientific,
825 Edison, New Jersey) (excitation wavelength, 485 nm; emission wavelengths, 505-530 nm; slit
826 width, 1 nm). To determine the maximum dye release, vesicles were lysed by adding 5 μL of 1%
827 (v/v) Triton X-100. The % leakage at time t was determined using the following equation:

828

829 $$\%\, leakage = \frac{I_t - I_0}{I_{max} - I_0} \times 100\% \qquad \text{(Eq. 7)}$$

830

831 where I_t is the fluorescence emission intensity at time t, I_0 is the intensity at time 0, and I_{max} is
832 the maximal intensity determined after detergent lysis of the vesicles (intensity values were
833 determined at 515 nm).

834

835 **AFM analysis of aSyn amyloid-like fibrils.** A mica surface functionalized with 1-(3-
836 aminopropyl) silatrane (APS) was used to image aSyn amyloid-like fibrils by AFM (18, 85-87).
837 APS-mica was prepared by incubating freshly cleaved mica in a solution of APS (167 μM) for 30
838 min and then rinsed with deionized water and dried with an argon stream. A suspension of aSyn
839 fibrils (10 μL, prepared as described above under 'aSyn fibrillization' with an incubation time of
840 ~100 h and diluted 1/20 in deionized water) was deposited onto the APS-mica surface, and the
841 sample was incubated for 2 min, rinsed with deionized water, and dried under an argon stream.
842 The sample was imaged with an AFM Nanoscope VIII system (Bruker, Santa Barbara, CA)

843 using MSNL probes (Cantilever F with spring constant 0.6 N/m), operating in air in peak force
844 mode. Images were acquired over a few randomly selected locations. Images were analyzed
845 using Gwyddion and FemtoScan online software (Advanced Technologies Center, Moscow,
846 Russia) (88, 89).
847
848 **TEM analysis of aSyn amyloid-like fibrils.** The morphology of aSyn amyloid-like fibrils
849 (prepared as described above under 'aSyn fibrillization' with an incubation time of ~100 h) was
850 analyzed by negative stain biological TEM (90). For biological sample preparation by negative
851 staining, which is a sample preparation technique that imparts the necessary contrast for
852 viewing during biological TEM imaging, 3 μL of aSyn sample solution (35 μM) was pipetted on a
853 discharged carbon-coated copper TEM grid substrate. Subsequently, the sample was washed
854 with deionized water carefully without letting it dry and stained with a 1% (w/v) phosphotungstic
855 acid solution (3 μL), which was left in contact with the protein on the grid for 1 min. The excess
856 solution was then removed by blotting with filter paper, and the sample was imaged using an
857 FEI Tecnai G2 20 Transmission Electron Microscope operating at 200 KV.
858
859 **Sample size estimation.** Samples sizes for studies of primary neuron viability, membrane-
860 induced aSyn aggregation, and aSyn-mediated membrane permeabilization were estimated via
861 power analysis based on our previous studies (16, 22). Power analyses were designed to
862 determine the number of biological replicates required to detect a ~20% or ~30% difference
863 from control, with $\alpha = 0.05$ (type I error) and power = 0.80 (statistical power). Biological
864 replicates are defined here as samples treated identically in independent experiments carried
865 out on different days. For *in vivo* experiments, sample sizes were estimated based on previous
866 data collected by our group and others for the A53T variant.
867

868 **Statistical analysis.** Statistical analyses were carried out using GraphPad Prism 6.0 (La Jolla,
869 CA). Primary neuron viability data, in vivo stereology and densitometry data, densitometry data
870 from Western blots, and calcein dye release data were analyzed via ANOVA followed by
871 Tukey's multiple comparisons *post hoc* test for normally distributed measurements. In analyzing
872 percentage dye release data and percentage cell viability data by ANOVA, square root
873 transformations were carried out to conform to ANOVA assumptions. Normalized FFN-102
874 fluorescence data were subjected to a log transformation to account for skewness in the data.
875 The log-transformed data were analyzed using an approach that accounts for comparison
876 across experiments conducted on different days. Log-transformed fluorescence emission values
877 for multiple treatment groups were compared using a general linear model implemented in the
878 GLM procedure of SAS Version 9.3 followed by Tukey's multiple comparisons *post hoc* test
879 (Cary, NC). Kruskal-Wallis followed by a Dunn's multiple comparisons test or a two-tailed Mann-
880 Whitney test were used as non-parametric tests. Differences were considered significant for
881 $p<0.05$. Unless otherwise stated, values of n indicated in the Figure Legends refer to the
882 number of independent biological replicates.
883

884 ## Acknowledgments

885 We thank Björn Anzelius, Anneli Josefsson, Ulla Samuelsson, and Ulrika Sparrhult-Björk (Lund
886 University) for excellent technical assistance and Aswathy Chandran (Purdue University) for
887 valuable discussions. We are also grateful to Dr. Christopher Gilpin (Purdue University) for
888 advice on TEM analyses.
889

890 ## References

891 1. Spillantini MG, Schmidt ML, Lee VM-Y, Trojanowski JQ, Jakes R, Goedert M. a-Synuclein
892 in Lewy bodies. Nature. 1997;388:839-40.

2. Petrucci S, Ginevrino M, Valente EM. Phenotypic spectrum of alpha-synuclein mutations: New insights from patients and cellular models. Parkinsonism & related disorders. 2016;22 Suppl 1:S16-20.
3. Deleersnijder A, Gerard M, Debyser Z, Baekelandt V. The remarkable conformational plasticity of alpha-synuclein: blessing or curse? Trends in molecular medicine. 2013;19(6):368-77.
4. Weinreb PH, Zhen W, Poon AW, Conway KA, Lansbury PT, Jr. NACP, a protein implicated in Alzheimer's disease and learning, is natively unfolded. Biochemistry. 1996;35(43):13709-15.
5. Theillet FX, Binolfi A, Bekei B, Martorana A, Rose HM, Stuiver M, et al. Structural disorder of monomeric alpha-synuclein persists in mammalian cells. Nature. 2016;530(7588):45-50.
6. Bartels T, Choi JG, Selkoe DJ. alpha-Synuclein occurs physiologically as a helically folded tetramer that resists aggregation. Nature. 2011;477(7362):107-10.
7. Giasson BI, Murray IV, Trojanowski JQ, Lee VM. A hydrophobic stretch of 12 amino acid residues in the middle of a-synuclein is essential for filament assembly. J Biol Chem. 2001;276(4):2380-6.
8. Dedmon MM, Lindorff-Larsen K, Christodoulou J, Vendruscolo M, Dobson CM. Mapping long-range interactions in alpha-synuclein using spin-label NMR and ensemble molecular dynamics simulations. Journal of the American Chemical Society. 2005;127(2):476-7.
9. Bertoncini CW, Jung YS, Fernandez CO, Hoyer W, Griesinger C, Jovin TM, et al. Release of long-range tertiary interactions potentiates aggregation of natively unstructured alpha-synuclein. P Natl Acad Sci USA. 2005;102(5):1430-5.
10. Levitan K, Chereau D, Cohen SI, Knowles TP, Dobson CM, Fink AL, et al. Conserved C-terminal charge exerts a profound influence on the aggregation rate of alpha-synuclein. J Mol Biol. 2011;411(2):329-33.
11. Bodner CR, Dobson CM, Bax A. Multiple tight phospholipid-binding modes of alpha-synuclein revealed by solution NMR spectroscopy. J Mol Biol. 2009;390(4):775-90.
12. Davidson WS, Jonas A, Clayton DF, George JM. Stabilization of alpha-synuclein secondary structure upon binding to synthetic membranes. J Biol Chem. 1998;273(16):9443-9.
13. Venda LL, Cragg SJ, Buchman VL, Wade-Martins R. alpha-Synuclein and dopamine at the crossroads of Parkinson's disease. Trends Neurosci. 2010;33(12):559-68.
14. Lee H-J, Choi C, Lee S-J. Membrane-bound a-synuclein has a high aggregation propensity and the ability to seed the aggregation of the cytosolic form. J Biol Chem. 2002;277:671-8.
15. Galvagnion C, Buell AK, Meisl G, Michaels TC, Vendruscolo M, Knowles TP, et al. Lipid vesicles trigger alpha-synuclein aggregation by stimulating primary nucleation. Nat Chem Biol. 2015;11(3):229-34.
16. Ysselstein D, Joshi M, Mishra V, Griggs AM, Asiago JM, McCabe GP, et al. Effects of impaired membrane interactions on alpha-synuclein aggregation and neurotoxicity. Neurobiol Dis. 2015;79:150-63.
17. Abedini A, Raleigh DP. A role for helical intermediates in amyloid formation by natively unfolded polypeptides? Phys Biol. 2009;6(1):15005.
18. Banerjee S, Hashemi M, Lv Z, Maity S, Rochet JC, Lyubchenko YL. A novel pathway for amyloids self-assembly in aggregates at nanomolar concentration mediated by the interaction with surfaces. Scientific reports. 2017;7:45592.
19. Reynolds NP, Soragni A, Rabe M, Verdes D, Liverani E, Handschin S, et al. Mechanism of membrane interaction and disruption by alpha-synuclein. J Am Chem Soc. 2011;133(48):19366-75.
20. Comellas G, Lemkau LR, Zhou DH, George JM, Rienstra CM. Structural intermediates during alpha-synuclein fibrillogenesis on phospholipid vesicles. J Am Chem Soc. 2012;134(11):5090-9.

943 21. Lee JH, Hong CS, Lee S, Yang JE, Park YI, Lee D, et al. Radiating amyloid fibril formation
944 on the surface of lipid membranes through unit-assembly of oligomeric species of alpha-
945 synuclein. PLoS ONE. 2012;7(10):e47580.
946 22. Ysselstein D, Dehay B, Costantino IM, McCabe GP, Frosch MP, George JM, et al.
947 Endosulfine-alpha inhibits membrane-induced alpha-synuclein aggregation and protects
948 against alpha-synuclein neurotoxicity. Acta neuropathologica communications. 2017;5(1):3.
949 23. Polymeropoulos MH, Lavedan C, Leroy E, Ide SE, Dehejia A, Dutra A, et al. Mutation in the
950 alpha-synuclein gene identified in families with Parkinson's disease. Science.
951 1997;276(5321):2045-7.
952 24. Ahlemeyer B, Halupczok S, Rodenberg-Frank E, Valerius KP, Baumgart-Vogt E.
953 Endogenous Murine Amyloid-beta Peptide Assembles into Aggregates in the Aged
954 C57BL/6J Mouse Suggesting These Animals as a Model to Study Pathogenesis of
955 Amyloid-beta Plaque Formation. J Alzheimers Dis. 2018;61(4):1425-50.
956 25. Kang L, Wu KP, Vendruscolo M, Baum J. The A53T mutation is key in defining the
957 differences in the aggregation kinetics of human and mouse alpha-synuclein. J Am Chem
958 Soc. 2011;133(34):13465-70.
959 26. Rochet JC, Conway KA, Lansbury PT, Jr. Inhibition of fibrillization and accumulation of
960 prefibrillar oligomers in mixtures of human and mouse a-synuclein. Biochemistry.
961 2000;39(35):10619-26.
962 27. Wu KP, Kim S, Fela DA, Baum J. Characterization of conformational and dynamic
963 properties of natively unfolded human and mouse alpha-synuclein ensembles by NMR:
964 implication for aggregation. J Mol Biol. 2008;378(5):1104-15.
965 28. Lo Bianco C, Ridet JL, Schneider BL, Deglon N, Aebischer P. alpha -Synucleinopathy and
966 selective dopaminergic neuron loss in a rat lentiviral-based model of Parkinson's disease.
967 Proc Natl Acad Sci U S A. 2002;99(16):10813-8.
968 29. Landeck N, Buck K, Kirik D. Toxic effects of human and rodent variants of alpha-synuclein
969 in vivo. The European journal of neuroscience. 2017;45(4):536-47.
970 30. Murray IV, Giasson BI, Quinn SM, Koppaka V, Axelsen PH, Ischiropoulos H, et al. Role of
971 alpha-synuclein carboxy-terminus on fibril formation in vitro. Biochemistry.
972 2003;42(28):8530-40.
973 31. Periquet M, Fulga T, Myllykangas L, Schlossmacher MG, Feany MB. Aggregated alpha-
974 synuclein mediates dopaminergic neurotoxicity in vivo. J Neurosci. 2007;27(12):3338-46.
975 32. Chen L, Periquet M, Wang X, Negro A, McLean PJ, Hyman BT, et al. Tyrosine and serine
976 phosphorylation of alpha-synuclein have opposing effects on neurotoxicity and soluble
977 oligomer formation. J Clin Invest. 2009;119(11):3257-65.
978 33. Negro A, Brunati AM, Donella-Deana A, Massimino ML, Pinna LA. Multiple phosphorylation
979 of a-synuclein by protein tyrosine kinase Syk prevents eosin-induced aggregation. FASEB
980 J. 2002;16(2):210-2.
981 34. Bassil F, Fernagut PO, Bezard E, Pruvost A, Leste-Lasserre T, Hoang QQ, et al. Reducing
982 C-terminal truncation mitigates synucleinopathy and neurodegeneration in a transgenic
983 model of multiple system atrophy. Proc Natl Acad Sci U S A. 2016;113(34):9593-8.
984 35. Winner B, Jappelli R, Maji SK, Desplats PA, Boyer L, Aigner S, et al. In vivo demonstration
985 that alpha-synuclein oligomers are toxic. Proc Natl Acad Sci U S A. 2011;108(10):4194-9.
986 36. Karpinar DP, Balija MB, Kugler S, Opazo F, Rezaei-Ghaleh N, Wender N, et al. Pre-fibrillar
987 alpha-synuclein variants with impaired beta-structure increase neurotoxicity in Parkinson's
988 disease models. Embo J. 2009;28(20):3256-68.
989 37. Bousset L, Pieri L, Ruiz-Arlandis G, Gath J, Jensen PH, Habenstein B, et al. Structural and
990 functional characterization of two alpha-synuclein strains. Nature communications.
991 2013;4:2575.

38. Gorman PM, Yip CM, Fraser PE, Chakrabartty A. Alternate aggregation pathways of the Alzheimer beta-amyloid peptide: Abeta association kinetics at endosomal pH. J Mol Biol. 2003;325(4):743-57.
39. Paleologou KE, Schmid AW, Rospigliosi CC, Kim HY, Lamberto GR, Fredenburg RA, et al. Phosphorylation at Ser-129 but not the phosphomimics S129E/D inhibits the fibrillation of alpha-synuclein. J Biol Chem. 2008;283(24):16895-905.
40. Sevcsik E, Trexler AJ, Dunn JM, Rhoades E. Allostery in a disordered protein: oxidative modifications to alpha-synuclein act distally to regulate membrane binding. J Am Chem Soc. 2011;133(18):7152-8.
41. Rieker C, Dev KK, Lehnhoff K, Barbieri S, Ksiazek I, Kauffmann S, et al. Neuropathology in mice expressing mouse alpha-synuclein. PloS one. 2011;6(9):e24834.
42. Fares MB, Maco B, Oueslati A, Rockenstein E, Ninkina N, Buchman VL, et al. Induction of de novo alpha-synuclein fibrillization in a neuronal model for Parkinson's disease. Proc Natl Acad Sci U S A. 2016;113(7):E912-21.
43. Burre J, Sharma M, Sudhof TC. Definition of a Molecular Pathway Mediating alpha-Synuclein Neurotoxicity. J Neurosci. 2015;35(13):5221-32.
44. Li Y, Liu W, Oo TF, Wang L, Tang Y, Jackson-Lewis V, et al. Mutant LRRK2(R1441G) BAC transgenic mice recapitulate cardinal features of Parkinson's disease. Nat Neurosci. 2009;12(7):826-8.
45. Goldberg MS, Pisani A, Haburcak M, Vortherms TA, Kitada T, Costa C, et al. Nigrostriatal dopaminergic deficits and hypokinesia caused by inactivation of the familial Parkinsonism-linked gene DJ-1. Neuron. 2005;45(4):489-96.
46. Fornai F, Schluter OM, Lenzi P, Gesi M, Ruffoli R, Ferrucci M, et al. Parkinson-like syndrome induced by continuous MPTP infusion: Convergent roles of the ubiquitin-proteasome system and {alpha}-synuclein. Proc Natl Acad Sci U S A. 2005;102(9):3413-8.
47. Burbulla LF, Song P, Mazzulli JR, Zampese E, Wong YC, Jeon S, et al. Dopamine oxidation mediates mitochondrial and lysosomal dysfunction in Parkinson's disease. Science. 2017;357(6357):1255-61.
48. Carballo-Carbajal I, Laguna A, Romero-Gimenez J, Cuadros T, Bove J, Martinez-Vicente M, et al. Brain tyrosinase overexpression implicates age-dependent neuromelanin production in Parkinson's disease pathogenesis. Nat Commun. 2019;10(1):973.
49. Paumier KL, Luk KC, Manfredsson FP, Kanaan NM, Lipton JW, Collier TJ, et al. Intrastriatal injection of pre-formed mouse alpha-synuclein fibrils into rats triggers alpha-synuclein pathology and bilateral nigrostriatal degeneration. Neurobiol Dis. 2015;82:185-99.
50. Lv G, Kumar A, Huang Y, Eliezer D. A Protofilament-Protofilament Interface in the Structure of Mouse alpha-Synuclein Fibrils. Biophys J. 2018;114(12):2811-9.
51. Hwang S, Fricke P, Zinke M, Giller K, Wall JS, Riedel D, et al. Comparison of the 3D structures of mouse and human alpha-synuclein fibrils by solid-state NMR and STEM. J Struct Biol. 2019;206(1):43-8.
52. Tanaka G, Yamanaka T, Furukawa Y, Kajimura N, Mitsuoka K, Nukina N. Sequence- and seed-structure-dependent polymorphic fibrils of alpha-synuclein. Biochimica et biophysica acta Molecular basis of disease. 2019;1865(6):1410-20.
53. Volpicelli-Daley LA, Luk KC, Patel TP, Tanik SA, Riddle DM, Stieber A, et al. Exogenous alpha-synuclein fibrils induce Lewy body pathology leading to synaptic dysfunction and neuron death. Neuron. 2011;72(1):57-71.
54. Luk KC, Kehm V, Carroll J, Zhang B, O'Brien P, Trojanowski JQ, et al. Pathological alpha-synuclein transmission initiates Parkinson-like neurodegeneration in nontransgenic mice. Science. 2012;338(6109):949-53.
55. Conway KA, Harper JD, Lansbury PT, Jr. Fibrils formed *in vitro* from a-synuclein and two mutant forms linked to Parkinson's disease are typical amyloid. Biochemistry. 2000;39:2552-63.

1043 56. Luk KC, Covell DJ, Kehm VM, Zhang B, Song IY, Byrne MD, et al. Molecular and Biological
1044 Compatibility with Host Alpha-Synuclein Influences Fibril Pathogenicity. Cell reports.
1045 2016;16(12):3373-87.
1046 57. Hejjaoui M, Butterfield S, Fauvet B, Vercruysse F, Cui J, Dikiy I, et al. Elucidating the role of
1047 C-terminal post-translational modifications using protein semisynthesis strategies: alpha-
1048 synuclein phosphorylation at tyrosine 125. J Am Chem Soc. 2012;134(11):5196-210.
1049 58. Burai R, Ait-Bouziad N, Chiki A, Lashuel HA. Elucidating the Role of Site-Specific Nitration
1050 of alpha-Synuclein in the Pathogenesis of Parkinson's Disease via Protein Semisynthesis
1051 and Mutagenesis. J Am Chem Soc. 2015;137(15):5041-52.
1052 59. Burre J, Sharma M, Sudhof TC. alpha-Synuclein assembles into higher-order multimers
1053 upon membrane binding to promote SNARE complex formation. Proc Natl Acad Sci U S A.
1054 2014;111(40):E4274-83.
1055 60. Lv Z, Hashemi M, Banerjee S, Zagorski K, Rochet JC, Lyubchenko YL. Assembly of alpha-
1056 synuclein aggregates on phospholipid bilayers. Biochimica et biophysica acta Proteins and
1057 proteomics. 2019;1867(9):802-12.
1058 61. Woods WS, Boettcher JM, Zhou DH, Kloepper KD, Hartman KL, Ladror DT, et al.
1059 Conformation-specific binding of alpha-synuclein to novel protein partners detected by
1060 phage display and NMR spectroscopy. J Biol Chem. 2007;282(47):34555-67.
1061 62. Parkkinen L, O'Sullivan SS, Collins C, Petrie A, Holton JL, Revesz T, et al. Disentangling
1062 the relationship between lewy bodies and nigral neuronal loss in Parkinson's disease.
1063 Journal of Parkinson's disease. 2011;1(3):277-86.
1064 63. Raiss CC, Braun TS, Konings IB, Grabmayr H, Hassink GC, Sidhu A, et al. Functionally
1065 different alpha-synuclein inclusions yield insight into Parkinson's disease pathology.
1066 Scientific reports. 2016;6:23116.
1067 64. Tompkins MM, Hill WD. Contribution of somal Lewy bodies to neuronal death. Brain
1068 research. 1997;775(1-2):24-9.
1069 65. Tsika E, Moysidou M, Guo J, Cushman M, Gannon P, Sandaltzopoulos R, et al. Distinct
1070 region-specific alpha-synuclein oligomers in A53T transgenic mice: implications for
1071 neurodegeneration. J Neurosci. 2010;30(9):3409-18.
1072 66. Surmeier DJ, Obeso JA, Halliday GM. Selective neuronal vulnerability in Parkinson
1073 disease. Nat Rev Neurosci. 2017;18(2):101-13.
1074 67. Maingay M, Romero-Ramos M, Kirik D. Viral vector mediated overexpression of human
1075 alpha-synuclein in the nigrostriatal dopaminergic neurons: a new model for Parkinson's
1076 disease. CNS spectrums. 2005;10(3):235-44.
1077 68. Heise H, Celej MS, Becker S, Riedel D, Pelah A, Kumar A, et al. Solid-state NMR reveals
1078 structural differences between fibrils of wild-type and disease-related A53T mutant alpha-
1079 synuclein. J Mol Biol. 2008;380(3):444-50.
1080 69. Lemkau LR, Comellas G, Lee SW, Rikardsen LK, Woods WS, George JM, et al. Site-
1081 specific perturbations of alpha-synuclein fibril structure by the Parkinson's disease
1082 associated mutations A53T and E46K. PloS one. 2013;8(3):e49750.
1083 70. Yonetani M, Nonaka T, Masuda M, Inukai Y, Oikawa T, Hisanaga S, et al. Conversion of
1084 wild-type alpha-synuclein into mutant-type fibrils and its propagation in the presence of
1085 A30P mutant. J Biol Chem. 2009;284(12):7940-50.
1086 71. Volles MJ, Lansbury PT, Jr. Vesicle permeabilization by protofibrillar a-synuclein is
1087 sensitive to Parkinson's disease-linked mutations and occurs by a pore-like mechanism.
1088 Biochemistry. 2002;41:4595-602.
1089 72. Volles MJ, Lee S-J, Rochet J-C, Shtilerman MD, Ding TT, Kessler JC, et al. Vesicle
1090 permeabilization by protofibrillar a-synuclein: implications for the pathogenesis and
1091 treatment of Parkinson's disease. Biochemistry. 2001;40(26):7812-9.
1092 73. Ma H, Yankee TM, Hu J, Asai DJ, Harrison ML, Geahlen RL. Visualization of Syk-antigen
1093 receptor interactions using green fluorescent protein: differential roles for Syk and Lyn in

1094 the regulation of receptor capping and internalization. Journal of immunology (Baltimore,
1095 Md : 1950). 2001;166(3):1507-16.
1096 74. Deng Y, Alicea-Velazquez NL, Bannwarth L, Lehtonen SI, Boggon TJ, Cheng HC, et al.
1097 Global analysis of human nonreceptor tyrosine kinase specificity using high-density peptide
1098 microarrays. Journal of proteome research. 2014;13(10):4339-46.
1099 75. Liu F, Hindupur J, Nguyen JL, Ruf KJ, Zhu J, Schieler JL, et al. Methionine sulfoxide
1100 reductase A protects dopaminergic cells from Parkinson's disease-related insults. Free
1101 Radic Biol Med. 2008;45(3):242-55.
1102 76. Grimm D, Kern A, Rittner K, Kleinschmidt JA. Novel tools for production and purification of
1103 recombinant adenoassociated virus vectors. Human gene therapy. 1998;9(18):2745-60.
1104 77. Zolotukhin S, Byrne BJ, Mason E, Zolotukhin I, Potter M, Chesnut K, et al. Recombinant
1105 adeno-associated virus purification using novel methods improves infectious titer and yield.
1106 Gene therapy. 1999;6(6):973-85.
1107 78. Schmitz C, Hof PR. Design-based stereology in neuroscience. Neuroscience.
1108 2005;130(4):813-31.
1109 79. West MJ. Stereological methods for estimating the total number of neurons and synapses:
1110 issues of precision and bias. Trends Neurosci. 1999;22(2):51-61.
1111 80. Gundersen HJ, Jensen EB. The efficiency of systematic sampling in stereology and its
1112 prediction. Journal of microscopy. 1987;147(Pt 3):229-63.
1113 81. Shvadchak VV, Falomir-Lockhart LJ, Yushchenko DA, Jovin TM. Specificity and kinetics of
1114 alpha-synuclein binding to model membranes determined with fluorescent excited state
1115 intramolecular proton transfer (ESIPT) probe. J Biol Chem. 2011;286(15):13023-32.
1116 82. Scholtz JM, Qian H, York EJ, Stewart JM, Baldwin RL. Parameters of helix-coil transition
1117 theory for alanine-based peptides of varying chain lengths in water. Biopolymers.
1118 1991;31(13):1463-70.
1119 83. Shvadchak VV, Yushchenko DA, Pievo R, Jovin TM. The mode of alpha-synuclein binding
1120 to membranes depends on lipid composition and lipid to protein ratio. FEBS Lett.
1121 2011;585(22):3513-9.
1122 84. Allen TM, Cleland LG. Serum-induced leakage of liposome contents. Biochimica et
1123 biophysica acta. 1980;597(2):418-26.
1124 85. Lovas S, Zhang Y, Yu J, Lyubchenko YL. Molecular mechanism of misfolding and
1125 aggregation of Abeta(13-23). The journal of physical chemistry B. 2013;117(20):6175-86.
1126 86. Lv Z, Condron MM, Teplow DB, Lyubchenko YL. Nanoprobing of the effect of Cu(2+)
1127 cations on misfolding, interaction and aggregation of amyloid beta peptide. Journal of
1128 neuroimmune pharmacology : the official journal of the Society on NeuroImmune
1129 Pharmacology. 2013;8(1):262-73.
1130 87. Lyubchenko YL, Shlyakhtenko LS. AFM for analysis of structure and dynamics of DNA and
1131 protein-DNA complexes. Methods (San Diego, Calif). 2009;47(3):206-13.
1132 88. Miyagi A, Ando T, Lyubchenko YL. Dynamics of nucleosomes assessed with time-lapse
1133 high-speed atomic force microscopy. Biochemistry. 2011;50(37):7901-8.
1134 89. Sun Z, Tan HY, Bianco PR, Lyubchenko YL. Remodeling of RecG Helicase at the DNA
1135 Replication Fork by SSB Protein. Scientific reports. 2015;5:9625.
1136 90. Brenner S, Horne RW. A negative staining method for high resolution electron microscopy
1137 of viruses. Biochimica et biophysica acta. 1959;34:103-10.

1138

1139 ## Figure Legends

1140 **Figure 1. Human and mouse aSyn have seven sequence mismatches.** (A) Sequence
1141 alignment of human, mouse, and chimeric aSyn variants showing mismatches between h-aSyn
1142 WT and m-aSyn at positions 53, 87, 100, 103, 107, 121, and 122. Also highlighted are the
1143 positions of familial PD substitutions and known serine and tyrosine phosphorylation sites. (B)
1144 Schematic representation of human, mouse, and chimeric aSyn variants examined in this study.

1145

1146 **Figure 2. Human/mouse mismatches at positions 121 and 122 affect aSyn neurotoxicity**
1147 **in cell culture.** Primary midbrain cultures were transduced with adenovirus encoding human,
1148 mouse, and chimeric aSyn variants at MOIs adjusted to ensure equal expression levels.
1149 Additional cultures were untransduced ('control'). The cells were fixed, stained with antibodies
1150 specific for MAP2 and TH, and scored for dopaminergic cell viability. The data are presented as
1151 the mean ± SEM, n = 4 (A, B), n = 5 (C), or n = 3 (D-F). *p<0.05, **p<0.01, ***p<0.001; square
1152 root transformation, one-way ANOVA followed by Tukey's multiple comparisons *post hoc* test.

1153

1154 **Figure 3. Human/mouse mismatches at positions 121 and 122 affect aSyn-mediated**
1155 **dopaminergic cell death in rat midbrain.** Rats (4-10 per group) were injected unilaterally into
1156 the SN with vectors encoding h-aSyn A53T, h-aSyn Chimera, m-aSyn, or m-aSyn Chimera at
1157 two different titers (1.3E13 gc/ml or 3.5E14 gc/ml). Eight weeks after surgery, coronal midbrain
1158 sections of the high-dose group were stained for aSyn in order to visualize transgene
1159 expression (A-E). Adjacent specimens were stained for TH (F-J), VMAT2 (K-O), Hu (P-T) or
1160 cresyl violet (U-Y). The first panel in each row shows a representative image of the contralateral
1161 uninjected side (A, F, K, P, U). Counts of TH+ nigral dopaminergic neurons are shown in Z for
1162 the lower vector dose and in AA for the higher vector dose. Data are presented as the

1163 percentage of intact side cell numbers ± SEM. **p<0.01; two-tailed Mann-Whitney U test. Scale
1164 bar, 50 μm (panels A-Y). *See also Figure S1*.
1165
1166 **Figure 4. Mouse-to-human substitutions at positions 121 and 122 enhance the ability of**
1167 **m-aSyn to elicit dopaminergic fiber loss in rat striatum.** Representative striatal rat brain
1168 sections stained for TH or VMAT2 (4-6 per group) are shown in panels A-E or G-K, respectively,
1169 as low-magnification images, and in panels A'-E' or G'-K', respectively, as corresponding high-
1170 magnification images. The imaged sections were from animals injected with the highest vector
1171 dose. The first panel of each row shows a representative image of the contralateral uninjected
1172 side (A, A', G, G'). Quantified staining intensities of the striatum are displayed in F for TH and L
1173 for VMAT2. Data are presented as the percentage of corresponding contralateral staining
1174 intensity ± SEM. *p<0.05; two-tailed Mann-Whitney U test. Scale bar, 1 mm (panels A-K) or 50
1175 μm (panels A'-K'). *See also Figure S2.*
1176
1177 **Figure 5. M-aSyn forms amyloid-like fibrils with a shorter lag time compared to human**
1178 **and chimeric aSyn variants.** The formation of amyloid-like fibrils was monitored in solutions of
1179 monomeric h-aSyn WT, h-aSyn A53T, and m-aSyn (A), or h-aSyn A53T, h-aSyn Chimera, m-
1180 aSyn Chimera, and m-aSyn (B) (35 μM of each). The protein solutions were incubated at 37 °C
1181 with constant agitation and analyzed at various times for thioflavin T fluorescence. The graphs
1182 show the mean normalized fluorescence (determined from 3 independent experiments; 3
1183 technical replicates per experiment) plotted against the incubation time. The dotted lines above
1184 and below each solid line correspond to the mean signal ± SEM. *See also Figure S3.*
1185
1186 **Figure 6. Human, mouse, and chimeric aSyn variants form amyloid-like fibrils with similar**
1187 **dimensions but different morphologies.** (A-D) Results of AFM analysis of fibrils prepared
1188 from recombinant h-aSyn A53T (A), m-aSyn (B), h-aSyn Chimera (C), and m-aSyn Chimera (D).

1189 Panels A(i) – D(i) on the left show typical AFM topographic images of fibrils formed by each
1190 aSyn variant. Dashed boxes indicate areas shown at a higher magnification in a spectral color
1191 scheme in panels A(ii) – D(ii). Panels A(iii)-D(iii) on the right show cross-section profiles.
1192 Regions of the fibrils from which the profiles are taken are shown with white solid lines on the
1193 AFM images in panels A(ii)-D(ii). Twisted fibrils were observed for m-aSyn (B) and h-aSyn
1194 Chimera (C). Twisted and non-twisted fibrils account for 65% and 35% (respectively) of total
1195 fibrils formed by m-aSyn, and 76% and 24% (respectively) of total fibrils formed by h-aSyn
1196 Chimera. Cross-section profiles in panels A(iii) and D(iii) reveal heights of non-twisted fibrils (~8-
1197 11 nm). Cross-section profiles 1 and 2 reveal heights of twisted fibrils at valley regions (~7-9
1198 nm) and peak regions (~11-12 nm), respectively, in panels B(iii) and C(iii). (E, F) Histograms
1199 showing distances between peaks of twisted fibrils formed by m-aSyn (E) and h-aSyn Chimera
1200 (F). The distances were determined from cross-section profiles obtained along the long axis of
1201 the fibrils. (G-L) Representative TEM images of fibrils formed by h-aSyn WT (G), h-aSyn A53T
1202 (H), m-aSyn (I), h-aSyn Chimera (J), and m-aSyn Chimera (K). Scale bar, 100 nm. (L) Higher-
1203 magnification images generated from boxed regions of panels G, I, and J show a pair of fibrils
1204 wound around each other via a helical twist (I), two fibrils aligned in parallel (II), or individual
1205 fibrils with a twisted morphology (III and IV).
1206
1207 **Figure 7. Human/mouse mismatches at positions 121 and 122 affect membrane-induced**
1208 **aSyn aggregation and aSyn-mediated vesicle disruption.** (A) Solutions of recombinant aSyn
1209 variants were incubated with increasing concentrations of SUVs composed of egg PG:PC (1:1
1210 mol:mol) and analyzed by far-UV CD to determine $[\theta]_{MR,222}$. The data were fit to equation 3 (see
1211 'Experimental Procedures'), and values for KD, minimum $[\theta]_{MR,222}$, and maximum α-helical
1212 content were determined from the values of the fit parameters (Table S1). (B) Monomeric aSyn
1213 variants were incubated with PG:PC SUVs (protein-to-lipid ratio, 1:20 mol/mol) at 37 °C for 72 h.
1214 Left: Representative Western blot image (the vertical line to the right of the image shows the

1215 region of the blot with bands corresponding to oligomeric forms of aSyn). Right: Bar graph
1216 showing the ratio of total oligomer band intensity to monomer band intensity determined for
1217 each sample. (C) Calcein-loaded SUVs were incubated in the absence ('ctrl') or presence of
1218 aSyn variants. Calcein release was monitored via fluorescence measurements using excitation
1219 and emission wavelengths of 485 nm and 515 nm, respectively. Left: graph showing % dye
1220 release versus time, with 100% release determined as the signal obtained from vesicles treated
1221 with Triton X-100. Right: table listing P values determined for vesicle permeabilization data
1222 obtained at the 120 h time point (a more complete listing of P values at different time points is
1223 presented in Table S2). The data in (B) and (C) are presented as the mean ± SEM, n = 4 (B) or
1224 n = 3 (C). *$p<0.05$, **$p<0.01$, ***$p<0.001$, ****$p<0.0001$, one-way ANOVA followed by Tukey's
1225 multiple comparisons *post hoc* test (a square root transformation was carried out on the data in
1226 panel C).

Figure 1

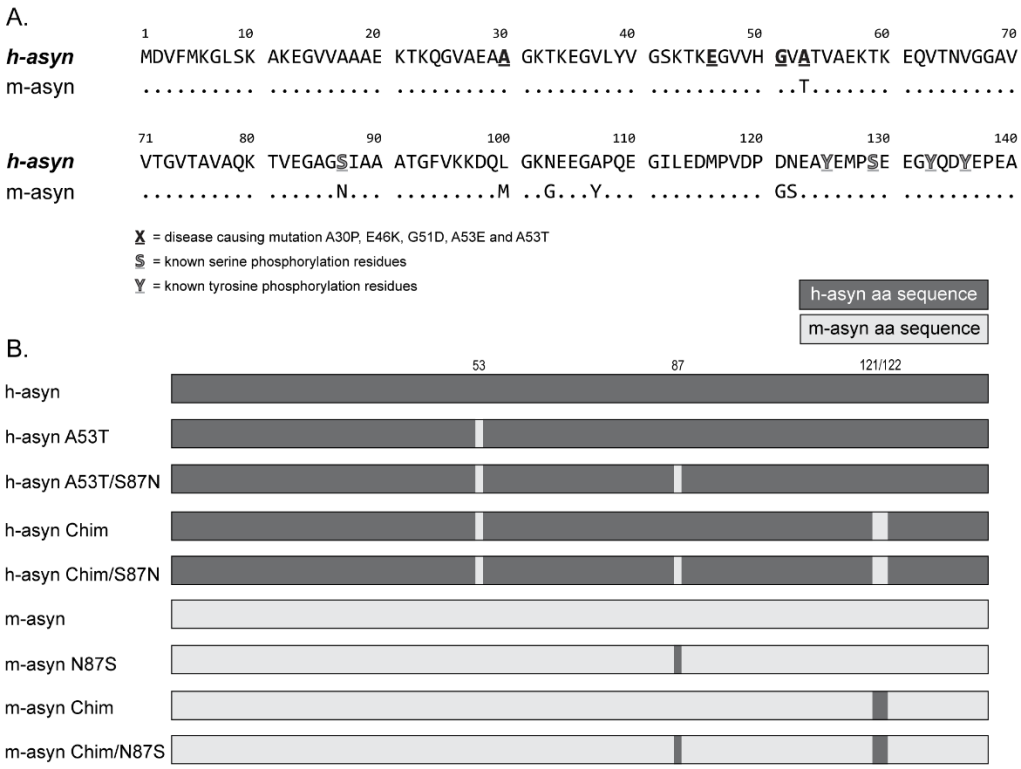
A.
1 10 20 30 40 50 60 70
h-asyn MDVFMKGLSK AKEGVVAAAE KTKQGVAEAA GKTKEGVLYV GSKTKEGVVH GVATVAEKTK EQVTNVGGAV
m-asyn ....T..... .....
71 80 90 100 110 120 130 140
h-asyn VTGVTAVAQK TVEGAGSIAA ATGFVKKDQL GKNEEGAPQE GILEDMPVDP DNEAYEMPSE EGYQDYEPEA
m-asyn ....N... .....M ..G...Y... ..... GS..... .....
X = disease causing mutation A30P, E46K, G51D, A53E and A53T
S = known serine phosphorylation residues
Y = known tyrosine phosphorylation residues
h-asyn aa sequence
m-asyn aa sequence
B.
53
87
121/122
h-asyn
h-asyn A53T
h-asyn A53T/S87N
h-asyn Chim
h-asyn Chim/S87N
m-asyn
m-asyn N87S
m-asyn Chim
m-asyn Chim/N87S

Figure 2

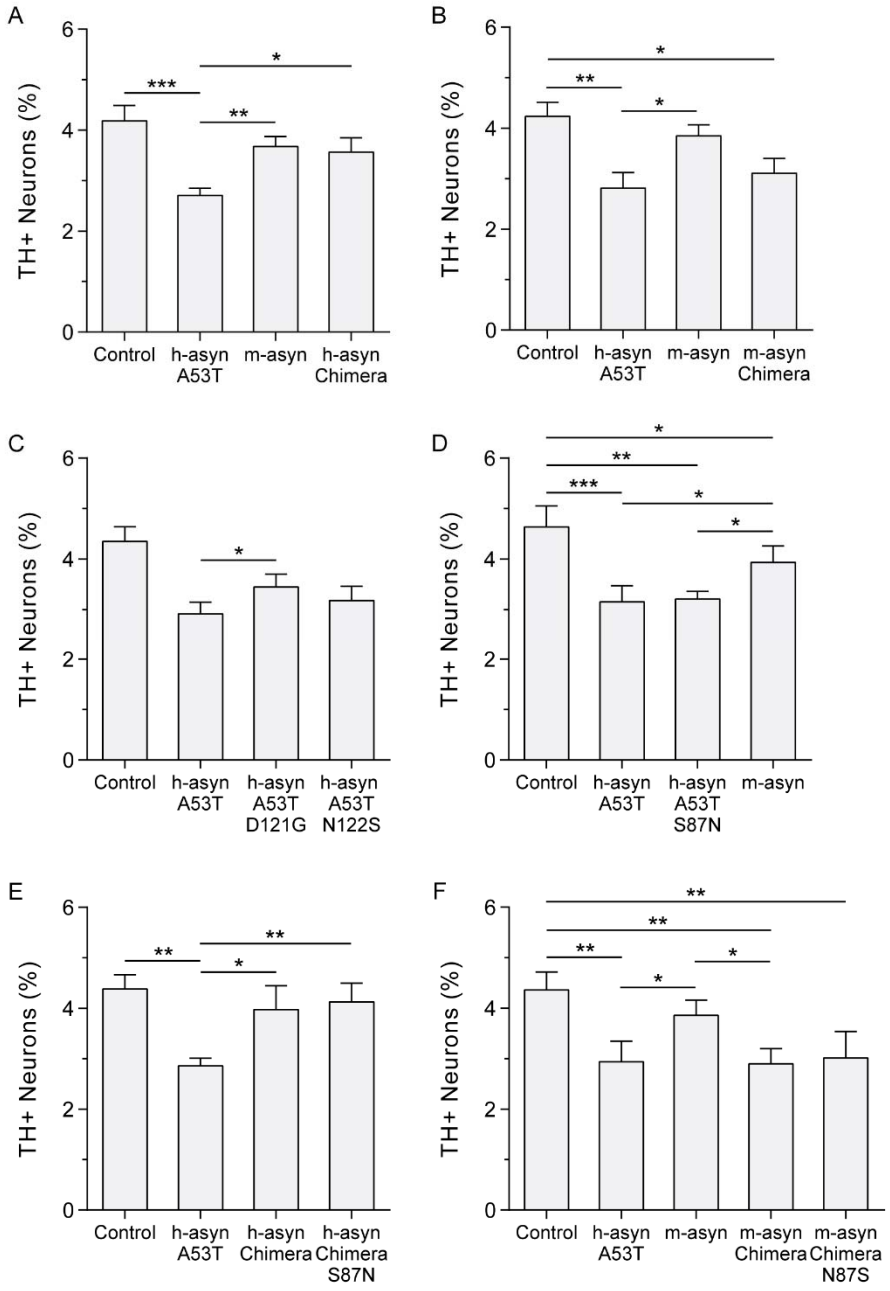
A
TH+ Neurons (%)
0
2
4
6
***
**
*
Control
h-asyn A53T
m-asyn
h-asyn Chimera
B
TH+ Neurons (%)
**
*
*
Control
h-asyn A53T
m-asyn
m-asyn Chimera
C
TH+ Neurons (%)
*
Control
h-asyn A53T
h-asyn A53T D121G
h-asyn A53T N122S
D
TH+ Neurons (%)
***
**
*
*
*
Control
h-asyn A53T
h-asyn A53T S87N
m-asyn
E
TH+ Neurons (%)
**
*
**
Control
h-asyn A53T
h-asyn Chimera
h-asyn Chimera S87N
F
TH+ Neurons (%)
**
**
**
*
*
Control
h-asyn A53T
m-asyn
m-asyn Chimera
m-asyn Chimera N87S

Figure 3

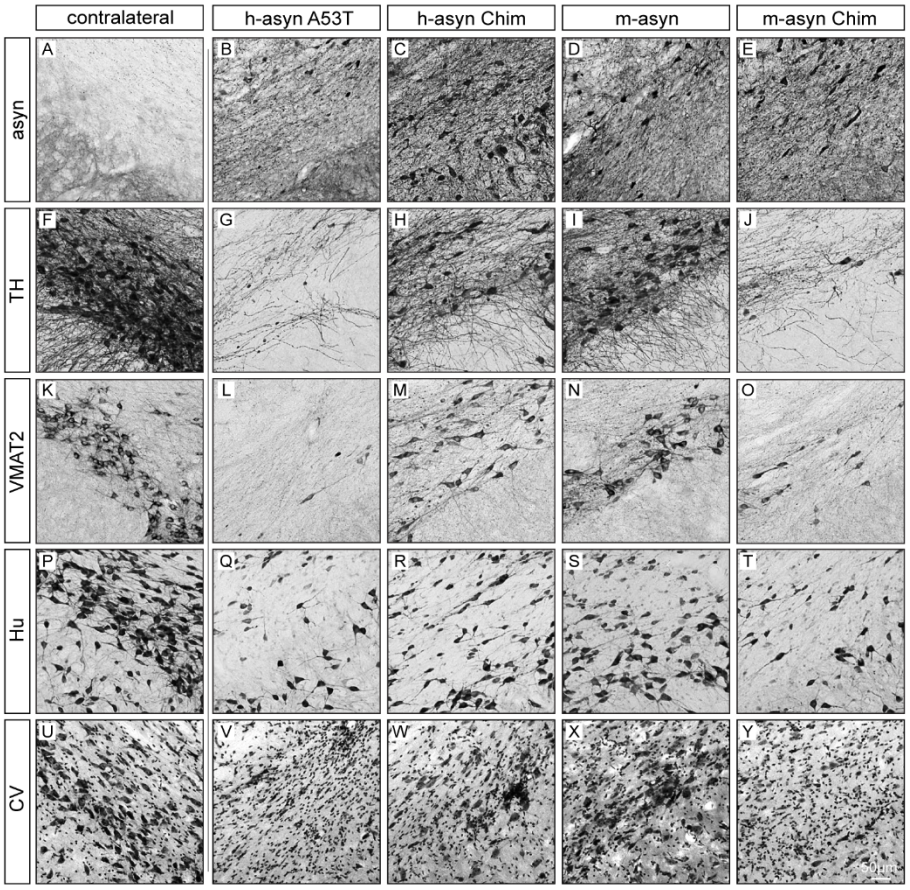
contralateral
h-asyn A53T
h-asyn Chim
m-asyn
m-asyn Chim
asyn
TH
VMAT2
Hu
CV
A
B
C
D
E
F
G
H
I
J
K
L
M
N
O
P
Q
R
S
T
U
V
W
X
Y

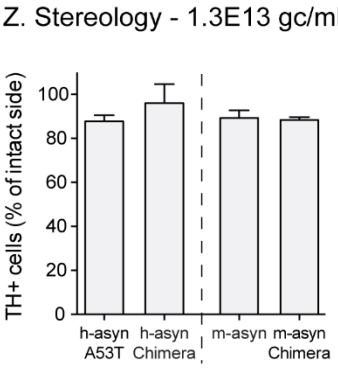
Z. Stereology - 1.3E13 gc/ml
TH+ cells (% of intact side)
100
80
60
40
20
0
h-asyn A53T
h-asyn Chimera
m-asyn
m-asyn Chimera

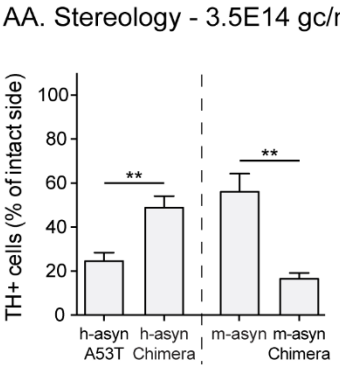
AA. Stereology - 3.5E14 gc/ml
TH+ cells (% of intact side)
100
80
60
40
20
0
**
**
h-asyn A53T
h-asyn Chimera
m-asyn
m-asyn Chimera

Figure 4

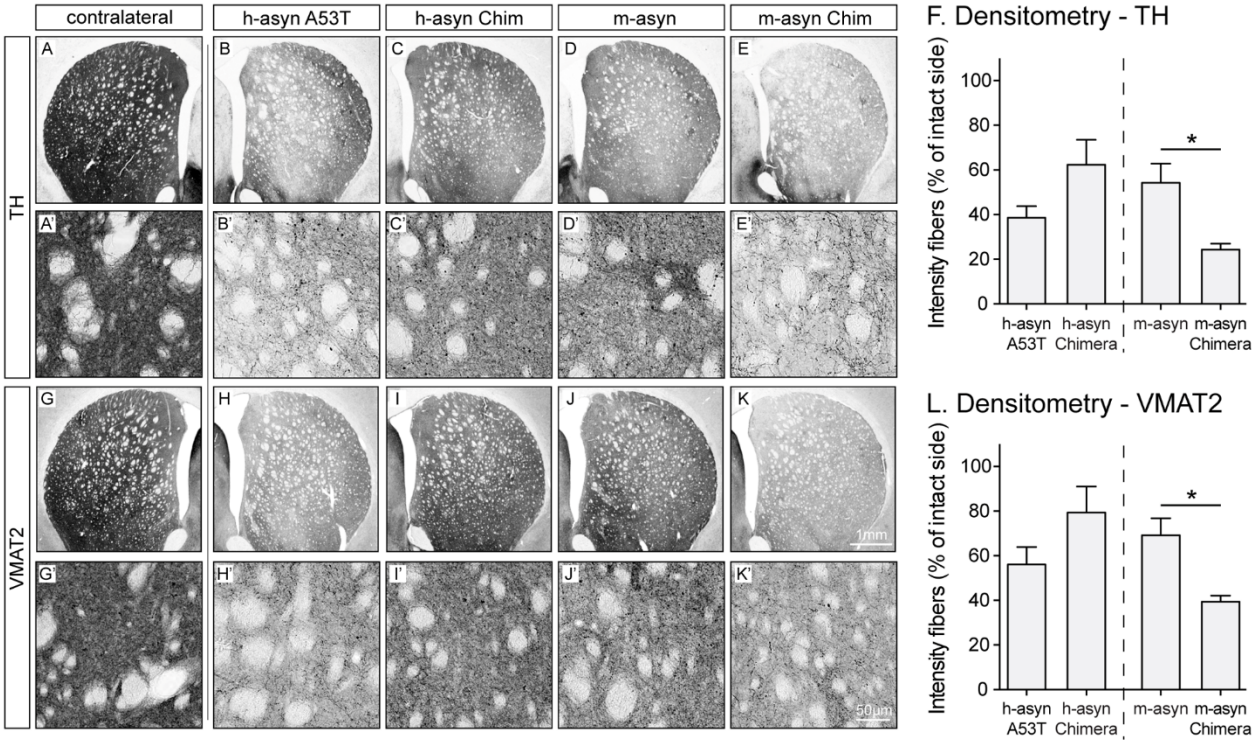
contralateral
h-asyn A53T
h-asyn Chim
m-asyn
m-asyn Chim
TH
VMAT2
A
B
C
D
E
A'
B'
C'
D'
E'
G
H
I
J
K
G'
H'
I'
J'
K'
1mm
50µm
F. Densitometry - TH
Intensity fibers (% of intact side)
100
80
60
40
20
0
*
h-asyn A53T
h-asyn Chimera
m-asyn
m-asyn Chimera
L. Densitometry - VMAT2
Intensity fibers (% of intact side)
100
80
60
40
20
0
*
h-asyn A53T
h-asyn Chimera
m-asyn
m-asyn Chimera

Figure 5.

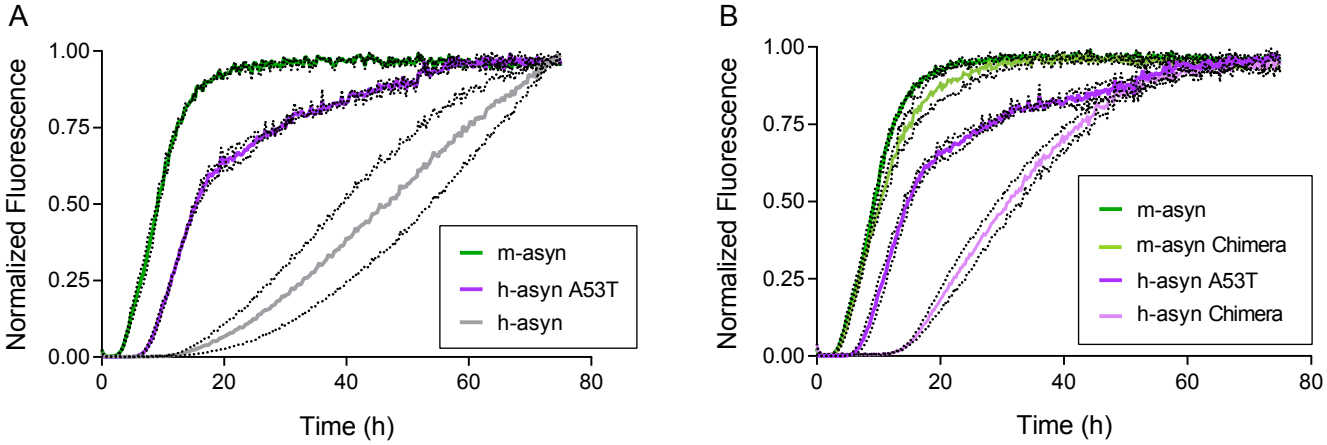
A
Normalized Fluorescence
1.00
0.75
0.50
0.25
0.00
0
20
40
60
80
Time (h)
m-asyn
h-asyn A53T
h-asyn
B
Normalized Fluorescence
1.00
0.75
0.50
0.25
0.00
0
20
40
60
80
Time (h)
m-asyn
m-asyn Chimera
h-asyn A53T
h-asyn Chimera

Figure 6

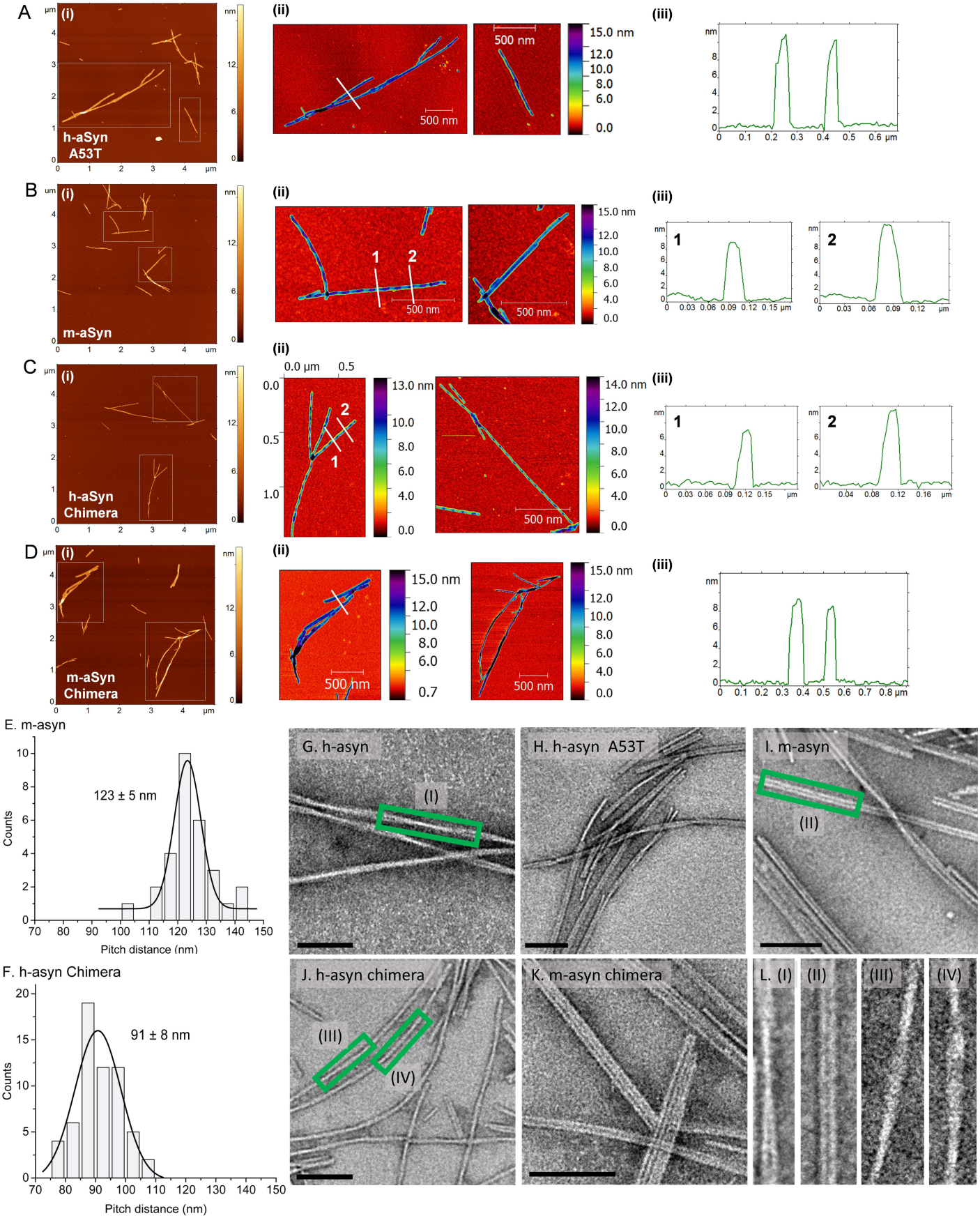
A
(i)
h-aSyn
A53T
(ii)
500 nm
15.0 nm
12.0
10.0
8.0
6.0
0.0
(iii)
B
m-aSyn
1
2
4.0
C
h-aSyn
Chimera
0.0 µm
0.5
1.0
13.0 nm
14.0 nm
D
m-aSyn
Chimera
0.7
E. m-asyn
123 ± 5 nm
Counts
Pitch distance (nm)
F. h-asyn Chimera
91 ± 8 nm
G. h-asyn
H. h-asyn A53T
I. m-asyn
J. h-asyn chimera
K. m-asyn chimera
L. (I)
(II)
(III)
(IV)

Figure 7

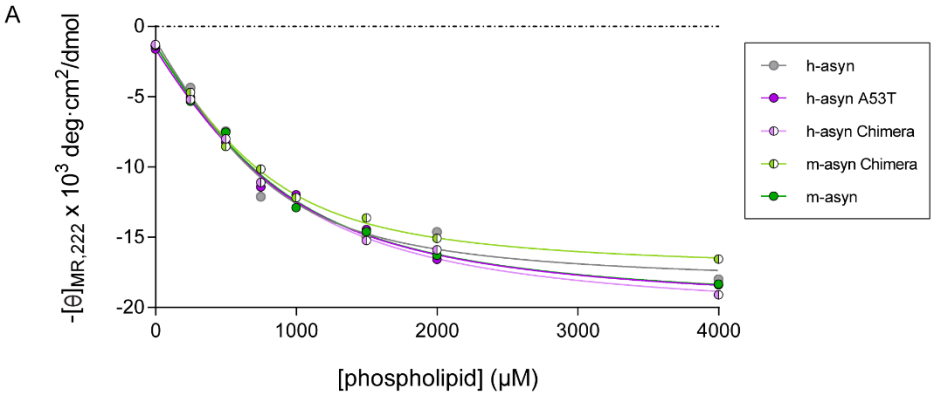

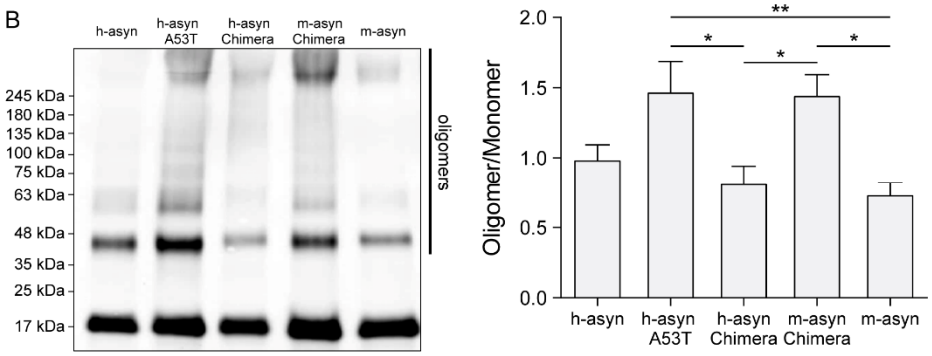

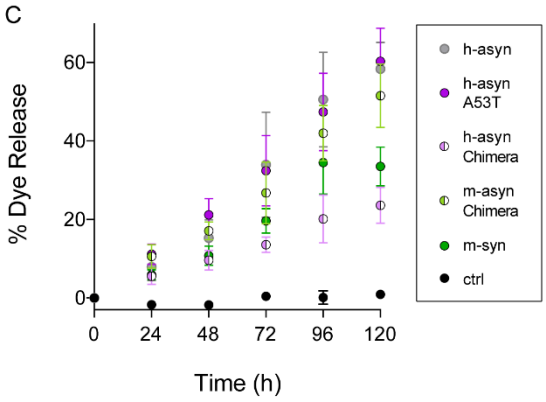

Comparison	Time (h) 120
h-asyn vs. h-asyn A53T	ns
h-asyn vs. m-asyn Chimera	ns
h-asyn vs. h-asyn Chimera	****
h-asyn vs. m-asyn	****
h-asyn A53T vs. m-asyn Chimera	ns
h-asyn A53T vs. h-asyn Chimera	****
h-asyn A53T vs. m-asyn	****
m-asyn Chimera vs. h-asyn Chimera	****
m-asyn Chimera vs. m-asyn	***
h-asyn Chimera vs. m-asyn	*